ABSTRACT

COMBUSTION SOOT NANOPARTICLES:
MECHANISM OF RESTRUCTURING AND MECHANICAL PROPERTIES

by
Ali Hasani

Soot, a product of incomplete combustion of fossil fuels, is a global warming agent. The effect of soot particles on climate depends on their morphology. Freshly released soot particles are fractal lacey aggregates, but they often appear collapsed in atmospheric samples collected away from emission sources. A body of work has concluded that the collapse is caused by liquid shells when they form by vapor condensation around soot aggregates. However, some recent studies argue that soot remains fractal even when engulfed by the shells, collapsing only when the shells evaporate. To reconcile this disagreement, the effects of the condensation and evaporation on restructuring are separated in this study, by anchoring coated and coated-denuded soot, after condensation and condensation-evaporation, respectively. The morphology of the particles collected in both ways is characterized by using scanning electron microscopy images. It is shown that wetting and non-wetting liquids act differently in soot restructuring. Liquids capable of wetting the surface of soot aggregates can induce a significant restructuring by condensation. With non-wetting liquids, such as water, it is the evaporation that drives most of restructuring and there is almost no restructuring during condensation.

Fractal soot particles released by combustion are typically hydrophobic, but can become hydrophilic after acquiring a coating layer made of hygroscopic atmospheric chemicals. To determine if absorption of water vapor by a thin hygroscopic coating can result in soot particle compaction at moderate relative humidities, the morphological

response of soot thinly coated with hygroscopic chemicals is investigated upon humidification. Mass-mobility analysis, scanning electron microscopy, and condensation models confirm that even under subsaturated conditions capillary condensation of hygroscopic chemicals can occur into the junctions between carbon spherules, driven by the saturation pressure depression caused by the concave menisci. Furthermore, the concave menisci promote absorption of a significant amount of water vapor by the condensate at moderate relative humidities, exceeding the amounts achievable for flat and convex surfaces. Results imply that exposure of fractal soot particles to subsaturated vapors of hygroscopic chemicals in the atmosphere may be an important route towards soot compaction even at moderate relative humidities.

The mechanistic details of soot aggregate restructuring remain poorly understood. In this study, atomic force microscopy is used for force-displacement measurements on bare, coated, and coated-denuded soot aggregates to determine their mechanical properties. The force curve is determined by measuring the deflection of the cantilever as it approaches and retracts from the sample. Peaks observed in the distributions of forces for bare soot may be related to the processes that occur during aggregate stretching, such as detachments between the monomers, unfolding, and breaking of the connection between monomers. These forces are significantly affected in the presence of a condensate. These results are expected to contribute to the development of physical models for soot restructuring.

Overall, the findings of this dissertation advance understanding of the processes governing the transformations and environmental impacts of soot that will benefit the experimental and modeling atmospheric research communities.

COMBUSTION SOOT NANOPARTICLES:
MECHANISM OF RESTRUCTURING AND MECHANICAL PROPERTIES

by
Ali Hasani

A Dissertation
Submitted to the Faculty of
New Jersey Institute of Technology
in Partial Fulfillment of the Requirements for the Degree of
Doctor of Philosophy in Chemistry

Department of Chemistry and Environmental Science

December 2022

APPROVAL PAGE

COMBUSTION SOOT NANOPARTICLES:
MECHANISM OF RESTRUCTURING AND MECHANICAL PROPERTIES

Ali Hasani

Dr. Alexei Khalizov, Dissertation Advisor	Date
Associate Professor of Chemistry and Environmental Science, NJIT	

Dr. Hao Chen, Committee Member	Date
Professor of Chemistry and Environmental Science, NJIT	

Dr. Zafar Iqbal, Committee Member	Date
Professor of Chemistry and Environmental Science, NJIT	

Dr. Lev Krasnoperov, Committee Member	Date
Professor of Chemistry and Environmental Science, NJIT	

Dr. Yuan Gao, Committee Member	Date
Professor of Earth and Environmental Sciences, Rutgers, Newark, NJ	

BIOGRAPHICAL SKETCH

Author: Ali Hasani

Degree: Doctor of Philosophy

Date: December 2022

Undergraduate and Graduate Education:

- Doctor of Philosophy in Chemistry,
  New Jersey Institute of Technology, Newark, NJ, 2022

- Master of Science in Chemical Engineering,
  Ferdowsi University, Mashhad, Iran, 2015

- Bachelor of Science in Chemical Engineering,
  Islamic Azad University, Iran, 2012

Major: Chemistry

Presentations and Publications:

Ali Hasani, Egor Demidov, and Alexei Khalizov, "Different mechanisms of soot restructuring by wetting and non-wetting liquids", American Chemical Society (ACS) Northeast Regional Meeting, Rochester, NY, 2-6 October 2022.

Ogochukwu Enekwizu, Ali Hasani, and Alexei Khalizov, "Vapor condensation and coating evaporation are both responsible for soot aggregate restructuring", Environmental Science and Technology. 2021, 55, 13, 8622–8630

Ali Hasani, Egor Demidov, and Alexei Khalizov, "Different mechanisms of soot restructuring by wetting and non-wetting liquids", American Geophysical Union (AGU) Fall Meeting 2021, New Orleans, LA, 13-17 December 2021, id. A55O-1596.

Ali Hasani, Egor Demidov, and Alexei Khalizov, "Does coating evaporation contribute to restructuring of soot aggregates?" Regional Meeting on Kinetics and Dynamics, 2021.

Ali Hasani, Ogochukwu Enekwizu, and Alexei Khalizov, "The interplay between capillary condensation and full encapsulation in the collapse of fractal soot particles," American Physical Society (APS), 2020.

Ali Hasani, Ogochukwu Enekwizu, and Alexei Khalizov, "The interplay between capillary condensation and encapsulation in the collapse of fractal soot particles," American Geophysical Union (AGU), 2020.

Ali Hasani, Ogochukwu Enekwizu, and Alexei Khalizov, "The interplay between capillary condensation and encapsulation in the collapse of fractal soot particles," Regional Meeting on Kinetics and Dynamics, Massachusetts Institute of Technology, Cambridge, MA, 2020.

تقدیم به سرزمین مادری‌ام، ایران، تقدیم به مادر، پدر و خواهر عزیزم.

To my motherland, Iran, to my dear mom, dad, and sister.

ACKNOWLEDGMENT

Many people constantly supported me to accomplish this dissertation and due to those people, my graduate experience has been one I will treasure forever.

First and foremost, I would like to express my deepest gratitude to my advisor, Dr. Alexei Khalizov, for his mentorship and instruction. With brilliance, enthusiasm, and patience, he inspired me to move my research forward. I am grateful for his suggestion about my presentation and writing skills.

I would like to show my gratitude to all committee members: Dr. Hao Chen, Dr. Zafar Iqbal, Dr. Lev Krasnoperov, and Dr. Yuan Gao for the suggestion to improve my research plan and my dissertation.

I would like to show my gratitude to my labmates, Dr. Ogo Enekwizu, Dr. Na Mao, Divjyot Singh, Egor Demidov, and Laurence Lu for their helpful suggestions, patience, encouragement, and most of all support for my research.

I would like to acknowledge the support from Dr. Gennady Gor and his research group, especially Ella Ivanova.

I would like to acknowledge the the support from the people in York center, Dr. Larisa Krishtopa, Dr. Xueyan Zhang, and, Dr. Lingfen Rao.

I wish to extend my special thanks to my family and my friends, Dung Ngoc Pham, Jose Antunes, and Sumbel Yaqoob, who always listen, understand, and believe in me. Their support and care helped me overcome stressful times and keep focusing on my study.

TABLE OF CONTENTS

LIST OF TABLES

LIST OF FIGURES

Figure   **Page**

Figure   **Page**

CHAPTER 1

INTRODUCTION

1.1 Motivation

Most of the energy produced for industry and transportation is derived from combustion of various carbon-containing fuels. Combustion inefficiencies result in the production of pollutants such as soot, which is a potent climate-warming agent, since it contains elemental carbon, a highly light absorbing substance (He, 2019). Soot particles are morphologically complex, existing as branched-chain aggregates of graphitic monomers, which can be arranged in an open (Figure 1.1a) or compact configuration (Figure 1.1b). The configuration of soot aggregate has a significant effect on its properties and atmospheric lifetime (Slowik et al., 2007).
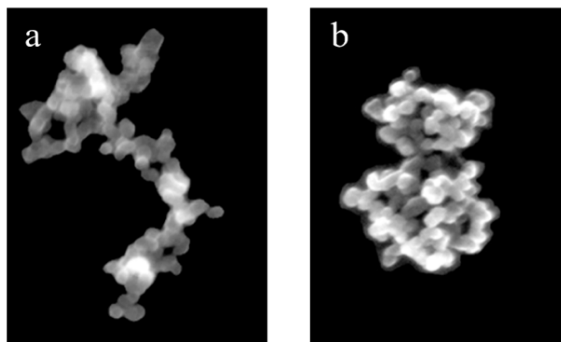
Figure 1.1 Soot aggregate: (a) open, and (b) compact configuration.

Once emitted to the atmosphere, soot is subjected to several aging processes, including oxidation, coagulation, and condensation of gaseous species. Typically, when a coating layer forms on the aggregate, the monomers become forced into a closer configuration. After acquiring a sufficient coating layer, the aggregate collapses to a compact globule (Schnitzler et al., 2017). Restructuring depends on the amount and the

properties of the coating material, including the surface tension, viscosity, and hygroscopicity (Schnitzler et al., 2017). For instance, hygroscopic coatings uptake water vapor and promote restructuring (Khalizov et al., 2009). Also, the distribution of the coating material over the aggregate is one of the key factors that control morphological changes (Chen et al., 2018). Considering the rate of restructuring, possible scenarios can be the instantaneous aggregate restructuring or kinetically slow restructuring when compared with the timescale of coating formation by vapor condensation.

As a major environmental pollutant, negative impacts of soot on air quality, human health, and climate warming, both in magnitude and temporal duration, depends strongly on the structure of soot nanoparticles (Zhang et al., 2008). Despite the growing body of research, the dynamics of restructuring and the factors controlling soot restructuring are not well explored and understood. Improved understanding of the mechanism and rate of restructuring of combustion soot nanoparticles is crucial to devising effective mitigation strategies to reduce uncertainties in climate predictions.

1.2 Atmospheric Aerosols: Sources and Impacts

Soot is an example of aerosol, which is defined as small liquid or solid particles suspended in air. Aerosols can be generated naturally or because of human activities as shown in Figure 1.2. Generally, aerosols are divided into two types: primary and secondary. Primary aerosols are atmospheric particles that are emitted directly into the atmosphere (Zelenyuk & Imre, 2005). For instance, in the form of ash particles or soot, they can be emitted as a product of combustion. Sea salt particles produced by breaking waves or dust carried by the wind are other examples of primary aerosols. Secondary aerosols are formed in the atmosphere by chemical reactions on the primary aerosols, such as the creation of sulfuric

acid droplets and sulfate particles from an initial injection of sulfur dioxide gas from volcanic eruptions (Lopez-Hilfiker et al., 2014). Aging and transformation of aerosols occur as they are transmitted through the atmosphere (Bzdek & Johnston, 2010). Particles with larger size are expected to deposit quickly. On the other hand, the atmospheric lifetime of the particles smaller than 1 micrometer reaches weeks and so they can be transported over oceans and continents (Kolb & Worsnop, 2012).
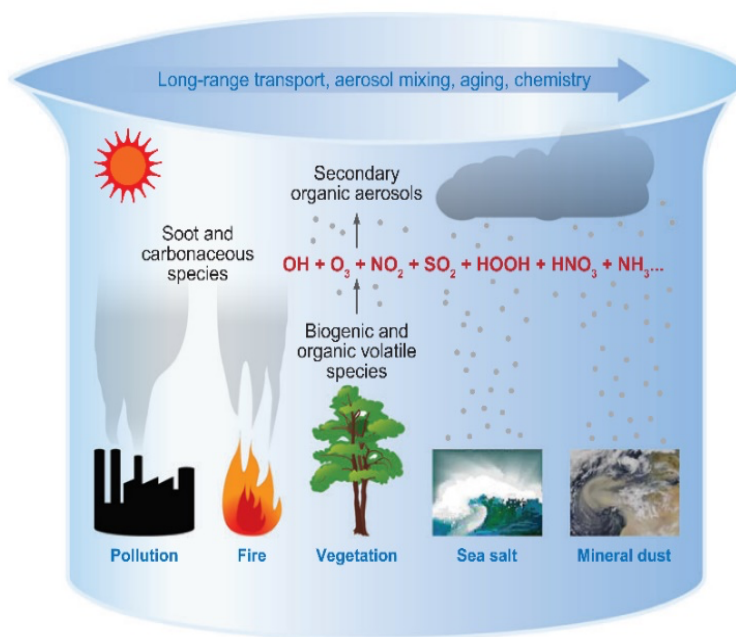
Figure 1.2 Examples of aerosol generation, aging, transformation, and transport in the atmosphere.
Source: (Bzdek & Johnston, 2010).

Aerosols have impacts on **air quality**, **human health**, and **climate**. Fine aerosol particles (<2.5 µm) act as a considerable **air pollutant**. Increasing the concentration of these particles not only decreases regional visibility, but also is a threat to human health. Inhalation of aerosols can exacerbate the impact of gaseous pollutants, such as ozone. In comparison with the larger particles, smallest ones are more probable to penetrate in the

pulmonary region and diffuse into the bloodstream (Burnett et al., 2014). Also, the gas composition of the atmosphere may change by the chemical reactions that occur in the bulk of aerosol particles or on their surface. For instance, the conversion of inactive chlorine reservoir species to photochemically active species through heterogeneous reactions on particle surfaces is the cause for the decrease in the concentration of the stratospheric ozone, which serves as a UV shield (Moore et al., 1990).

The effect of aerosols on climate includes **direct** and **indirect** effects. Their direct effect is due to sunlight absorption and scattering. The nature of aerosol, whether it is mostly light absorbing or scattering, is quantified using a parameter called single scattering albedo (SSA), which is the ratio of the light scattering to the extinction (sum of scattering and absorption). A purely scattering particle has an SSA of unity, whereas a strongly absorbing particle has an SSA close to zero. Aerosol emitted from most sources, such as sea-salt spray, biogenic emissions, and some anthropogenic emissions (e.g., nitrates and sulfates), dominantly scatter light and cause cooling. Carbonaceous aerosols like soot dominantly absorb light and contribute to the warming of the atmosphere (Liu et al., 2017).

Considering indirect effect, aerosol particles can act as cloud condensation nuclei (CCN) for cloud droplets formation and therefore, indirectly affect climate. The introduction of a larger number of aerosols leads to generation of cloud droplets that are smaller in size but greater in number. These clouds reflect more light (cloud-albedo effect), leading to a cooling of the atmosphere. The ability of aerosol particles to serve as CCN depends on various factors such as the particle size, hygroscopicity, chemical composition, and the relative humidity (Twohy & Anderson, 2008).

Many different types of condensation nuclei are present in the atmosphere. Some become wetted at relative humidities (RH) less than 100% and account for the haze that impedes visibility. The large condensation nuclei are those that may grow to cloud droplet size. As moist air is cooled, the relative humidity approaches 100%. The more hygroscopic members of the nucleus population then begin to serve as centers of condensation. By continued cooling, supersaturation is produced and is depleted by the condensation on nuclei. Supersaturation means the excess of relative humidity over the equilibrium value of 100%. Thus, air with a relative humidity of 101.5% has a supersaturation of 1.5%. (Supersaturation = RH-100%). In clouds, there are usually enough nuclei present to keep the supersaturation from rising above about 1%. It is an important characteristic of the atmosphere that there are always condensation nuclei present to provide for cloud formation when the relative humidity barely exceeds 100% (Seinfeld & Pandis, 1998).

A certain minimum supersaturation is needed for a particle to grow by water vapor condensation into a cloud droplet. This particle's **critical supersaturation**, S_c, depends on its dry diameter and its chemical composition. This relationship has been described by **Köhler theory** (Köhler, 1936) based on the thermodynamic equilibrium between the aqueous solution droplet and the ambient water vapor, since atmospheric droplets contain dissolved compounds. The saturation ratio over an aqueous drop of a given solute concentration is defined by the **Köhler equation** (Equation 1.1) (Seinfeld & Pandis, 1998), as a ratio of the water vapor pressure over the droplet, $p_w(D_p)$, to the pure water vapor pressure over a flat surface, p^o, at the same temperature:

$$\ln(\text{RH}) = \ln\left(\frac{p_w(D_p)}{p^o}\right) = \frac{4 M_w \sigma_w}{RT \rho_w D_p} - \frac{6 i n_s M_w}{\pi \rho_w D_p^3} \qquad (1.1)$$

where M_w is the molecular weight of water, σ_w is the surface tension of water, R is the universal gas constant, T is temperature in Kelvin, ρ_w is the density of water, D_p is the droplet diameter, and n_s is the moles of solute. Also, there is an approximation of the Köhler equation to describe the dependence of saturation ratio on the size of a solution droplet (Equation 1.2).

$$\frac{p_w(D_p)}{p^o} = 1 + \frac{a}{r} - \frac{b}{r^3} \qquad a = \frac{2\sigma_w}{\rho_w RT} \qquad b = \frac{3iM_w m}{4\pi\rho_w M_s} \qquad (1.2)$$

In this approximate form, a/r is the "curvature term" which expresses the increase in saturation ratio over a spherical droplet as compared to a plane surface. The term b/r^3 is the "solution term" that shows the reduction in vapor pressure due to the presence of a dissolved substance. In b, i is the degree of ionic dissociation, and m is the mass of the solute, M_w and M_s are molecular weight of the water and solute respectively (Seinfeld & Pandis, 1998). In Köhler theory curvature term is counteracted by solution term. So, water vapor condensation can occur at a lower saturation ratio into a concave surface (negative curvature) with more solute. In the other words, decreasing the "curvature term" and increasing "solution term" would result in water vapor condensation at a lower saturation ratio.

1.3 Soot Formation and Morphology

The knowledge of soot formation helps to understand its morphology and chemical structure. Figure 1.3 illustrates a schematic of the transition of gas-phase molecules to soot nanoparticles through the chain reactions of resonance-stabilized radicals (RSR) (Johansson et al., 2015). These chain reactions of radicals begin with the primary molecules like benzene and acetylene, produced from the pyrolysis of the carbon-based fuels. Then,

these primary blocks are transformed into polycyclic aromatic hydrocarbons (PAHs) such as naphthalene and anthracene. After that, the chain of aromatic rings grows through a fast polymerization process by the replacement of hydrogen atoms with hydrocarbons such as C_2H_2 groups. An increase in the number of aromatic rings leads to the formation of the monomer spheres, a nucleus of a soot particle with the size of a few nanometers. Through additional condensation and coagulation, the monomer grows to reach the size of 10-50 nm (Johansson et al., 2018). Freshly generated soot monomers have almost spherical shape and they coagulate to form fractal chainlike structures (Bento et al., 2006). This coagulation leads to formation of an aggregate in which monomers are **point-touch** connected to each other (Figure 1.4a). On the other hand, continued surface growth of the monomers after coagulation leads to formation of the soot aggregates in which monomer spheres are connected to each other with **necks** (Figure 1.4b).
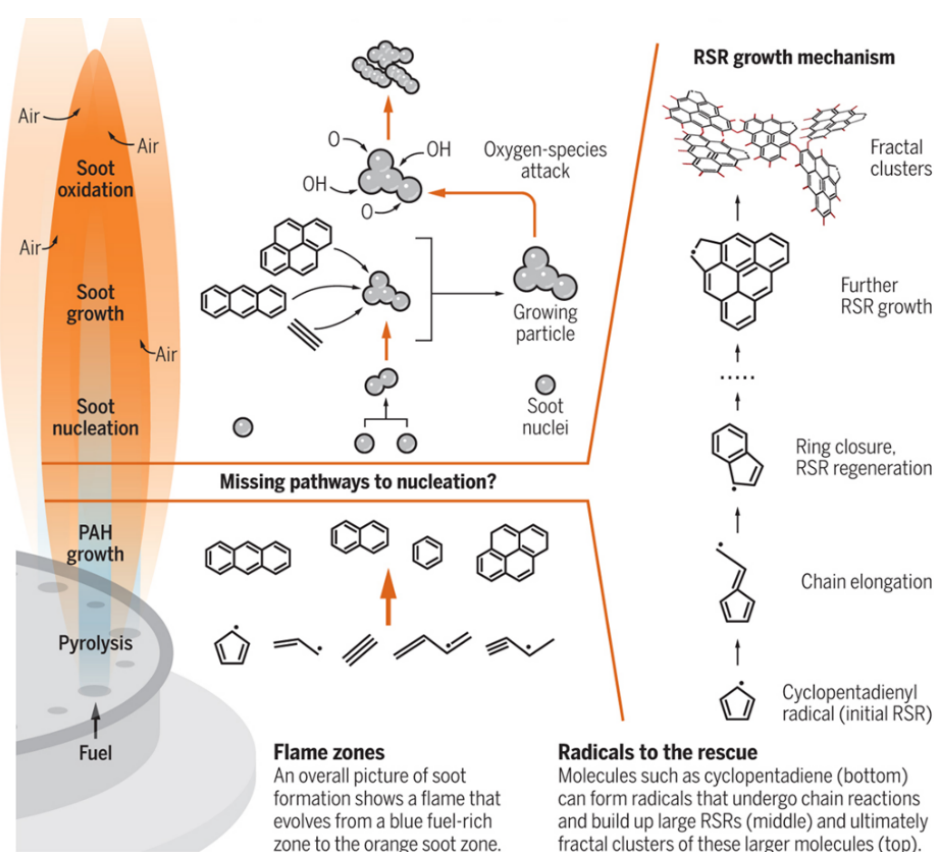
Figure 1.3 Transition of gas-phase molecules to soot nanoparticles through the chain reactions of resonance-stabilized radical (RSR).
Source: (Johansson et al., 2015).

a)   b)
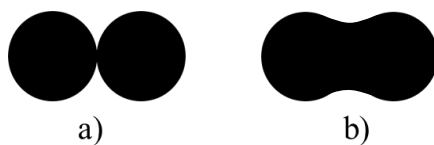
Figure 1.4 Monomer spheres connected; (a) without neck, (b) with neck.

The morphology (configuration of the monomers within an aggregate) of fresh soot aggregates is quantified using morphological parameters such as fractal dimension (D_f) and structural coefficient (k_a), roundness, convexity, radius of gyration (R_g), volume (V), and surface area (A_s) (China et al., 2015). The fractal dimension shows the morphology of aggregate based on mass-length relations, where each particle is represented as an

aggregate of same-sized primary spheres (monomers) and follows the fractal scaling law (Equation 1.3), in which N is the number of monomers, k_a is the prefactor (also called the structural coefficient), R_g is the radius of gyration, a is the monomer radius, and D_f is the fractal dimension. The fractal dimension increases during the restructuring of soot from fractal to a collapsed morphology. The fractal dimension of fresh soot aggregates is about 1.8, but increases to nearly 3 when the aggregate collapses to take a completely compact morphology (Sorensen, 2011). The radius of gyration R_g is the root-mean-square distance of monomer centers from the aggregate center of mass with position vector $\boldsymbol{r_c} = \frac{1}{N}\sum_{i=1}^{N}(\boldsymbol{r_i})$ and can be calculated by Equation (1.4), where $\boldsymbol{r_i}$ is the position of the center of the ith monomer.

$$N = k_a \left(\frac{R_g}{a}\right)^{D_f} \tag{1.3}$$

$$R_g^2 = \frac{1}{N}\sum_{i=1}^{N}(r_i - r_c)^2 \tag{1.4}$$

Convexity (Figure 1.5b) is the ratio of the projected area of the soot aggregate to that of an inscribing convex polygon. Roundness (Figure 1.5c) is the ratio of the projected area of a soot aggregate to that of the circle with the diameter of the maximum length of the aggregate. Fractal soot aggregate has a lower value of roundness and convexity in comparison with a compact aggregate (China et al., 2015).
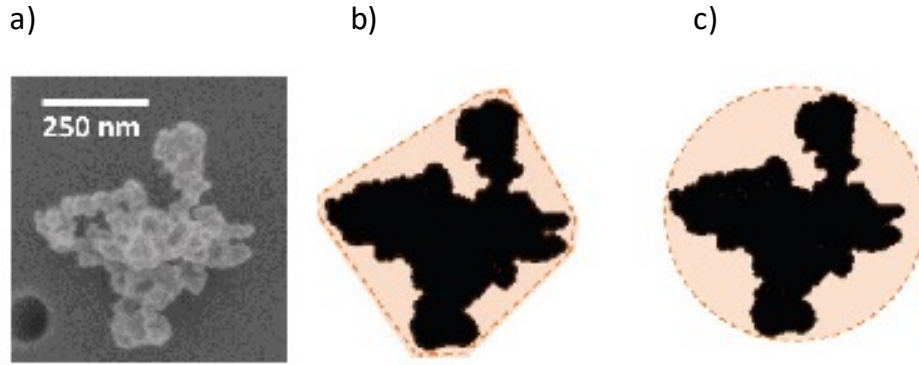
Figure 1.5 (a) SEM image of a soot aggregate, (b) Convexity =0.69, (c) Roundness =0.49. *Source: (Bhandari et al., 2019).*

The surface area A_s of a population of soot particles can be determined by measuring its reactivity with gases. For individual particles, V and A_s also can be evaluated from the diameter and number of monomers. However, the calculation for individual particles includes uncertainties such as contact area between monomers, accuracy of diameter and number of monomers (DeCarlo et al., 2004). An empirical formula relating the number of monomers (N_m) and the projected number of monomers (N_{proj}) has been proposed, where N_m can be corrected for an overlapping factor by Equation (1.5) (Chakrabarty et al., 2011; Scarnato et al., 2013).

$$N_m/N_{Proj} = 0.46 \, e^{0.68 D_f} \qquad (1.5)$$

In situ characterization of the airborne soot particles has been done using light scattering analysis to provide information on the morphology of the aggregates (Sorensen et al., 2018; Yon et al., 2018). Alternatively, water-engulfed soot particles can be directly injected into water medium for offline light scattering measurements (Ma et al., 2013). Light scattered intensity (I) versus wave vector (q) is the most fundamental measurement

for sizing. The magnitude of the wave vector q is an experimental parameter which is controlled by the scattering angle (θ) via Equation (1.6), in which λ is the wavelength of light. From the I versus q plot (Figure 1.6), one can in principle determine the aggregate radius of gyration (R_g), fractal dimension (D_f), and the monomer size (a) (Sorensen, 2001).

$$q = 4\pi\lambda^{-1}\sin(\theta/2) \tag{1.6}$$
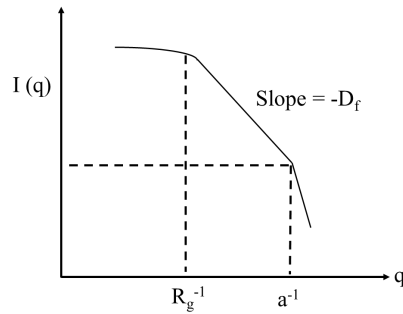
Figure 1.6 In scattered light intensity I (q) versus $q = 4\pi\lambda^{-1}\sin(\theta/2)$, θ is the scattering angle, R_g is the radius of gyration, a is the monomer size, and D_f is the fractal dimension of the soot aggregate.

Scanning electron microscopy (SEM) and transmission electron microscopy (TEM), are other ways to investigate the morphology of soot aggregates (Figure 1.7). Electron microscopy methods apply high magnification and high resolution to examine the collected particles, determine important details of their morphology and internal structure, and measure the real sizes of the agglomerates and monomers (Liati et al., 2014). As for a recent study on the impact of sampling medium on particle morphology, by collecting soot aggregates on silicon chips, it was possible to fix their morphology, even after coating evaporation (Chen et al., 2017). Knowing this fact, coated soot aggregates can be collected on silicon chips, and after coating evaporation, morphology of the coated soot aggregates can be characterized through electron microscopy.
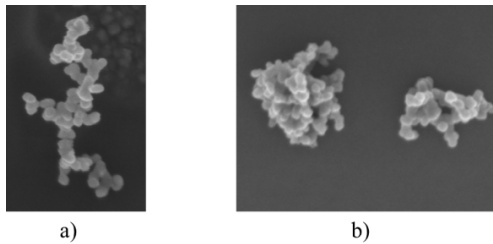
Figure 1.7 SEM images of 240 nm soot: (a) fractal, and (b) compact, after exposing to diethyl adipate. SEM imaging has been done at York center, New Jersey Institute of Technology.

Mass-mobility measurements: The differential mobility analyzer (DMA) continuously separates soot particles according to their migration velocities in an electric field with high resolution. The mobility can be related to particle size. Combined with a continuous-flow condensation particle counter (CPC), the DMA enables differential size distribution measurements (DeCarlo et al., 2004). The aerosol particle mass analyzer (APM) is an instrument to measure single aerosol particle mass based on the balance of centrifugal force and electrostatic force (Ehara et al., 1996). The APM is commonly operated with a DMA for the size-specific particle mass measurement with nearly real time resolution (McMurry et al., 2002).

Effective density from mass-mobility measurements: A common definition of effective density is the ratio of the measured particle mass to the particle volume calculated assuming a spherical particle with a diameter equal to the measured. The required parameters, mass, and diameter are obtained from a mass-mobility measurement. For instance, the DMA–APM setup can be used to perform this measurement. A DMA selects particles of a certain electrical mobility followed by downstream scanning of mass with an APM (McMurry et al., 2002).

Mass-mobility scaling exponent: by measuring the particle mobility diameter d_p, and mass m, over a range of mobility sizes, a power law relationship can be used to extract the mass-mobility scaling exponent D_m, which contains shape information of the aerosol population (Equation 1.7) (McMurry et al., 2002; Park et al., 2003).

$$m \propto d_p^{D_m} \tag{1.7}$$

1.4 Atmospheric Aging of Soot

As emitted into the atmosphere, soot particles are typically hydrophobic aggregates. During transport, soot undergoes various aging processes such as oxidation, coagulation with other aerosols, and condensation of gaseous species, resulting in changes in its morphology (particle size and shape) and properties (hydrophilicity, light absorption and scattering) (Koehler et al., 2009; Swarup et al., 2015). The hydrophilicity of soot particles can be enhanced with aging processes such as condensation of gaseous oxidized organics and H_2SO_4, or oxidation by OH, O_3, and HNO_3 (Zuberi et al., 2005). Hydrophilic soot particles can act as CCN at atmospherically relevant supersaturation conditions (Koehler et al., 2009).

The irregular geometry and complex microstructure of soot aggregates may provide active sites for deposition and condensation of water and other chemical species. These chemicals come from photochemical oxidation of volatile compounds, which leads to formation of low-volatility products. For example, pinonic acids have been suggested as important products from α-pinene reaction with ozone (Zhang & Zhang, 2005). Then these products absorb and deposit on the soot aggregate to form coating (Khalizov et al., 2009; Ma et al., 2013). The coating distribution over aggregate is mostly controlled by vapor

supersaturation of the condensing chemical that can be a uniform coating (for low volatile chemicals or high supersaturation) or between junctions of the spheres (for intermediate volatility chemicals or low supersaturation) (Figure 1.8) (Chen et al., 2018).

Figure 1.8 The coating distribution over aggregate can be (a) uniform coating or (b) between junctions of the spheres.

Usually, freshly generated soot is externally mixed with other aerosol particles. The term 'external mixture' indicates that soot aggregates individually and separately exist in a group of different airborne particles (Figure 1.9a). On the other hand, during aging, soot aggregates go thorough interaction with other inorganic and organic materials, in which through condensation or coagulation processes, internally mixed particles are formed. 'Internal mixture' is the mixing of two or more different kinds of aerosol materials in the same particle (Figure 1.9b). Considering the internally mixed, soot particles can be fully or partially coated with condensing materials. Also, they may be attached to the surface of other particles that coagulated with, or part of the soot particles penetrate inside the host material (Cheng et al., 2014).
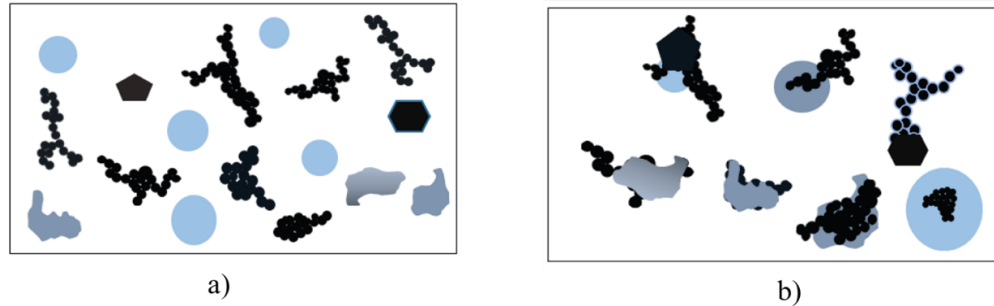
Figure 1.9 (a) external mixture, (b) internal mixture of soot (fractal black particles) with other aerosol materials.
Source: (Bhandari et al., 2019).

The optical properties of compact soot differ from the fractal soot. Based on laboratory experiments, when fractal soot collapses to a compact morphology it has ~5% higher absorption and ~100% higher scattering (Radney et al., 2014). Also, soot absorbs more light in association with other nonabsorbing aerosol compounds (e.g., sulfate). Figure 1.10b illustrates how internally mixed soot particles look in atmospheric samples. However, in climate models, such particles are considered in a simplified way, as a volume or mass equivalent core-shell configuration (Figure 1.10a). In the core-shell models, the soot core is placed at the center and the outer coating material acts as a "lens" refracting the light inward (Scarnato et al., 2013). Studies have shown that the "lensing" effect, caused by coating, enhances light absorption by the soot core, even with a completely non-absorbing coating material. Consequently, the warming effect by aged soot almost balances the net cooling effect of other anthropogenic aerosols. The absorption of solar radiation by internally mixed soot aerosols leads to warming in the middle atmosphere and reduces clouds over the tropics (Kahnert et al., 2014; Zhao & Ma, 2009).
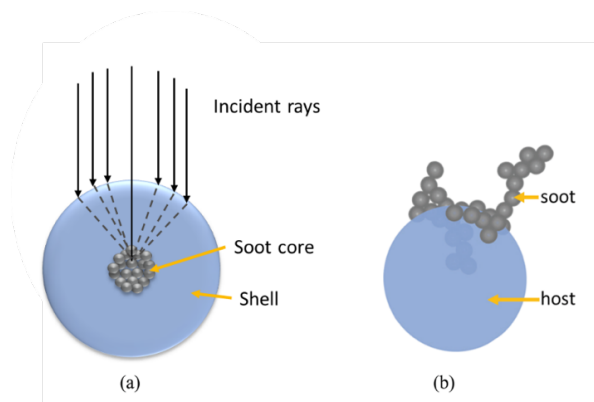
Figure 1.10 Schematic representation of (a) Core-shell model for a thickly coated soot and (b) surface-attached soot.
Source: (Kahnert et al., 2014).

1.5 The Mechanism of Soot Restructuring

The environmental impacts of soot considerably depend on its morphology and mixing state (mutual arrangement between the aggregate and its coating layer). For instance, the atmospheric lifetime is longer for open aggregates, because they experience a larger drag than compact particles. Also, compact aggregates scatter solar radiation more than open aggregates, resulting in reducing the effect of global warming. This significant effect of morphology on soot properties and atmospheric transformation has led to a growing body of research to figure out the changes in morphology of soot nanoparticles throughout atmospheric transformations (Liu et al., 2017).

The irregular geometry of the soot particles can be active sites for deposition of water and other chemical species. Fractal soot aggregates (Figure 1.7a) may collapse under the impact of the coating (deposited compounds) and restructure to a less fractal, more compact morphology (Figure 1.7b). Soot particles restructure due to surface tension of the condensate either during condensation (Schnitzler et al., 2017; Tritscher et al., 2011) or evaporation (Ebert et al., 2002; Ma et al., 2013). There exist strong claims that it is evaporation and not condensation that induces restructuring (Ebert et al., 2002; Ma et al.,

16

2013). Restructuring depends on several factors, including the amount and also the properties of the coating material, such as hygroscopicity. For instance, it has been reported that absorption of water vapor by hygroscopic coatings promotes restructuring (Khalizov et al., 2009). Also, the distribution of the coating material over the aggregate is considered as a key factor controlling morphological changes (Chen et al., 2018; Chen et al., 2016).

Soot restructuring can result from the **<u>capillary condensation</u>**, **<u>uniform condensation</u>**, or **<u>encapsulation</u>** of the soot aggregate. Capillary condensation, filling of cavities in the contact region of the primary spherules with condensate, occurs below saturation vapor pressure due to the Kelvin effect in which the vapor pressure above the concave surface is less than saturated vapor pressure. The contact angle 'φ', (Figure 1.11a) depends on the liquid coating chemical and the surface of the soot. Usually, a liquid with smaller surface tension is expected to have a smaller contact angle. The liquid phase facilitates the sliding of the primary spherules in the contact region. Considering a wetting liquid, the molecules creep along the surface, so the contact between spherules surfaces is replaced by liquid-liquid contact (Figure 1.11b). The capillary force in the cavities will exert torque on the primary spherules and cause them to rotate with respect to each other. This rotation will lead to compaction of a soot aggregate (Ma et al., 2013). Through this process, restructuring of the aggregates occurs. Going beyond capillary condensation, when the menisci grow very large to uniformly coat the aggregate, overlapping takes place at certain orientations of the primary spherules. Then an additional force, resulting from the surface tension of the liquid bridges, brings the primary spherules into a closer configuration so as to minimize the surface of the liquid phase (Kütz & Schmidt-Ott, 1992).

If supersaturation is high enough, liquid condensate forms a droplet encapsulating the soot aggregate. When the soot aggregate is immersed in liquid, sliding of the primary spherules is further promoted. When the vapor pressure of the coating liquid is decreased, evaporation occurs, the droplet shrinks, leading to soot restructuring (Figure 1.11c). This effect is expected to be related to the surface tension of the liquid (Kütz & Schmidt-Ott, 1992).
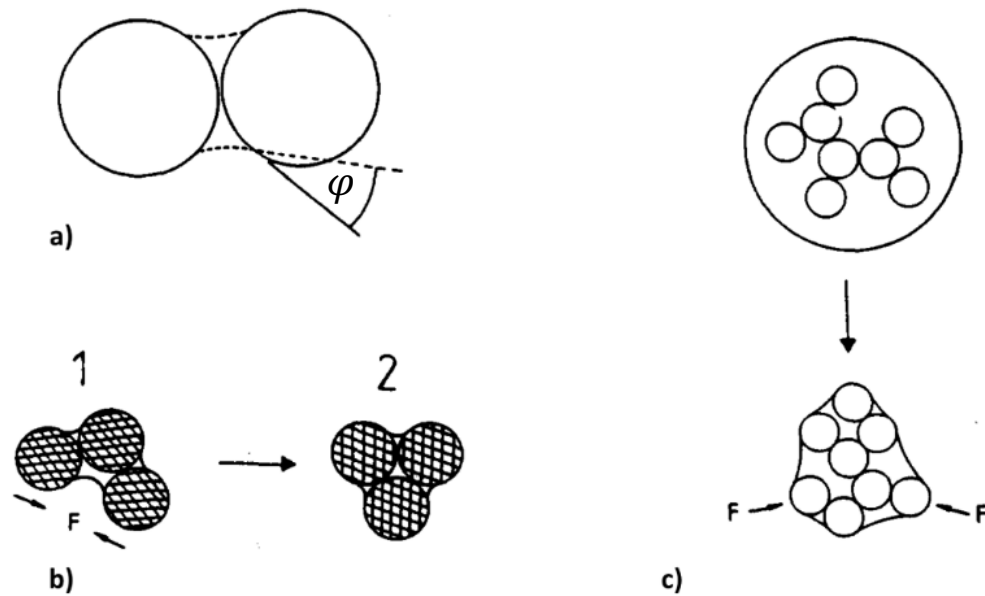
Figure 1.11 Different mixing state of soot aggregate and coating material.
Source: (Kütz & Schmidt-Ott, 1992).

As mentioned before, in some soot aggregates monomer spheres are connected to each other with carbon necks (Figure 1.12) (Doner et al., 2017). However, the effect of these necks on restructuring of soot aggregates is unexplored. These necks can hinder restructuring of the aggregate in two ways. First, the presence of these necks can limit capillary condensation, because cavities in the contact region of the primary spherules is occupied with necks. Second, even in the case of soot encapsulation, the parts of the

aggregate with necks do not restructure, since spherules are connected with necks, which are stronger than point-touch connections.
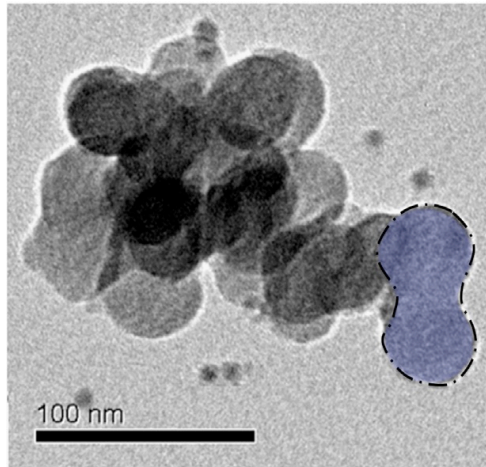
Figure 1.12 TEM image of a soot aggregate. An example of neck between monomers is marked.
Source: (Doner et al., 2017).

GOAL / OBJECTIVES

The major goal of this project is to elucidate and quantify the factors that control restructuring of combustion soot nanoparticles. Accordingly, several scientific questions will be answered by this dissertation:

- Is it condensation or evaporation of the coating material that triggers soot restructuring?

- How does subsaturated and supersaturated water vapor affect restructuring of the coated soot aggregates?

- How do interaction forces between the monomers in soot aggregate change when it is thinly/thickly coated or compact?

Major objectives of this project are:

1. Investigate soot aggregate restructuring upon exposure to intermediate volatility chemicals, to determine the extent of restructuring caused by capillary condensation in subsaturated vapor and relative roles of vapor condensation and coating evaporation on restructuring.

2. Investigate interaction of thinly coated soot particles with water vapor and determine the role of the subsaturated and supersaturated water vapor on restructuring of coated soot aggregates.

3. Measure force-displacement curves for soot aggregates subjected to different processing: bare fractal, thinly coated fractal, thickly coated, and bare compact to quantify the interaction forces between the monomers in bare, coated, and coated-denuded soot aggregates.

CHAPTER 2

METHODOLOGY

2.1 Aerosol Generation and Processing

Figure 2.1 shows a schematic of the system for aerosol generation, processing, and analysis. Soot particles were generated in an inverted diffusion burner by combustion of natural gas. Generated soot particles were sampled from the burner using an ejector dilutor, with particle-free air preheated to 150 °C to avoid water condensation. Also, in some experiments, an atomizer was used to generate spherical particles of polystyrene latex or ammonium sulfate. Diluted sample flow was dried in a diffusion dryer filled with silica gel followed by a Nafion dryer (Perma Pure, PD-07018T-24MSS), which were connected in series, lead to a relative humidity (RH) below 5%, as measured by a Vaisala HMM100 sensor. Before processing, soot particles are brought to an equilibrium charge distribution in a bipolar diffusion charger (Po-210, 400 µCi, NRD Staticmaster) and size classified in a differential mobility analyzer (DMA, TSI 3081). DMA is used to select particles of a specific size from a broad distribution (10-700 nm). It is operated at a 0.3 lpm sample flow and a sheath-to-sample flow ratio of 10. The size-classified soot particles are sent through a Pyrex saturator chamber, partly filled with liquid coating material (~20 mL) and maintained at a constant temperature by a proportional–integral–derivative (PID) controller.

After the chamber, temperature decreases and the sample flow cools down as traveling along the stainless-steel tubing, leading to condensation of supersaturated vapor, not only on the particles, but also on the tubing wall. If needed, the coating can be removed from

the particles by sending the sample flow through a thermal denuder (TD) maintained at 300 °C. Additionally, particles are collected electrostatically on silicon chips and lacy grids for SEM and TEM imaging, respectively.
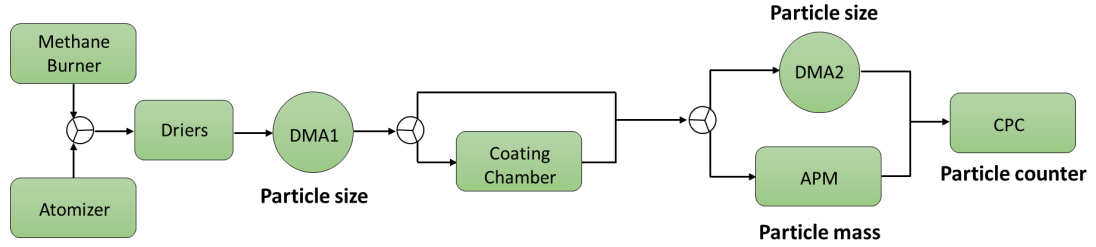
Figure 2.1 Schematic of the system for aerosol generation, processing and analysis.

2.2 Mass-Mobility Analysis

The electrical mobility diameter (d_m) is the diameter of a sphere with the same migration velocity in a constant electric field as the particle of interest (DeCarlo et al., 2004). Instruments such as the DMA measure d_m. This measurement is obtained via a force balance between the electrical force of a constant electric field on the net charges on the particle and the drag force experienced by the particle (Barone et al., 2003). Accordingly, the electrical mobility (Z_p) of a particle is defined as the ratio of the constant limiting velocity (v) a charged particle will reach in a uniform electric field to the magnitude of this field (E), $v = Z_p E$. The electrical mobility depends mainly on the particle size (mobility diameter) and electrical charge. The smaller the particle and/or the higher the electrical charge the higher is the electrical mobility. The electrical mobility is in general given in dependence of the particle mobility diameter d_m by Equation (2.1), in which n is the number of charges on the particle, e is the elementary unit of charge, C_c is the Cunningham slip

correction, which is size dependent, a correction to the friction for particles between the continuum and free molecular regime, and η is the gas viscosity.

$$Z_p = \frac{neC_c(d_m)}{3\pi\eta d_m} \qquad (2.1)$$

Mobility diameter and absolute mass of the particles are measured using a system comprising a DMA, an aerosol particle mass analyzer (APM, Kanomax 3601), and a condensation particle counter (CPC, TSI 3772). The voltage of the first DMA is maintained constant to select particles of a certain mobility diameter. Then, the size-classified particles are processed (coated or coated/denuded), as mentioned above. After that, the second DMA is used to scan the mobility diameter of processed particles. In order to measure bare or processed particle mass, sample flow is sent to the APM. In APM mass of the particle is obtained based on the balance between centrifugal force and electrostatic force by Equation (2.2), in which m is the particle mass, r is particle location relative to axis of rotation, ω is the APM angular speed, q is the particles charge, V is the applied voltage, and r_1, r_2 are radii of inner and outer electrodes.

$$mr\omega^2 = q\frac{V}{rln(\frac{r_2}{r_1})} \qquad (2.2)$$

To get mobility and mass distribution, voltage is scanned in the second DMA and APM, respectively, and the particle concentration at the exit of either is measured using CPC. Gfd and Gfm are used to describe relative changes in particle size and mass. Gfd = $d_{processed}/d_{initial}$ and Gfm = $m_{processed}/m_{initial}$, in which d is the particle mobility diameter and m is the particle mass. The subscripts "initial" and "processed" refer to the particles before and after processing (coated or coated/denuded).

2.3 Electron Microscopy Analysis

In the experiments, airborne particles (240 nm mobility diameter) were collected on silicon chips or lacy grids, using a custom-built electrostatic sampler (Chen et al., 2017; Dixkens & Fissan, 1999). Prior to particle collection, the surface of the silicon chips was washed and dried using methanol in an ultrasound bath and nitrogen gas, respectively. Then, cleaned silicon chips were placed in the electrostatic sampler, in which by applying high voltage 3-4 kV, airborne particles were collected on the surface of the silicon. The morphology of the collected particles was then characterized using scanning electron microscopy (SEM) (JSM-7900F) or transmission electron microscopy (TEM) images (JEM-F200), at York center, New Jersey Institute of Technology.

2.4 Atomic Force Microscopy Analysis

Atomic force microscopy (AFM) is a high-resolution type of scanning probe microscopy (SPM), offering the possibility to explore different kinds of surface properties (Miyahara et al., 1999). The AFM consists of a cantilever with a sharp tip (probe) that is used to scan the surface of the sample of study. During this process, the cantilever senses the interaction forces existing between the probe and the sample, that depending on the situation can be mechanical contact forces, van der Waals, electrostatic forces, etc., leading to a deflection of the cantilever. During this "contact" of the cantilever with the sample, the cantilever bends upwards while a certain force is applied to the sample. Typically, this deflection is measured using a laser spot reflected from the top surface of the cantilever into an array of photodiodes, and it is transformed into an electric signal, which is processed and delivered as topographic information of the sample point where the tip is placed. Since the system

has the ability to scan the surface, a topographic image of all the scanned area is obtained. A simplified AFM schematic is depicted in Figure 2.2.
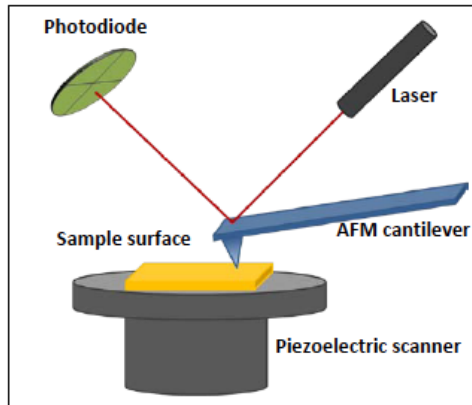
Figure 2.2 Schematics of an AFM. The sample is mounted on a piezo stage that allows movement on the X, Y and Z coordinates.

AFM not only is used to image sample topographies, but also is often employed to measure nanomechanical properties of surfaces as well. Force-displacement measurements is a straightforward and reliable technique to quantitatively study nanomechanical properties such as Young's modulus and adhesion force on a variety of samples (Ramirez-Aguilar et al., 1999; Rong et al., 2004). Figure 2.3 is a typical force-displacement curve recorded as the AFM tip approaches (gray line) and retracts (black line) from an aggregate-coated silicon substrate (Rong et al., 2004). The light gray curve represents the force acting on the tip as it moves toward the substrate surface (step 1), at the contact point (step 2), and while it is indented into the sample (step 3). The black line is the force acting on the tip as it moves away from the surface (step 4).
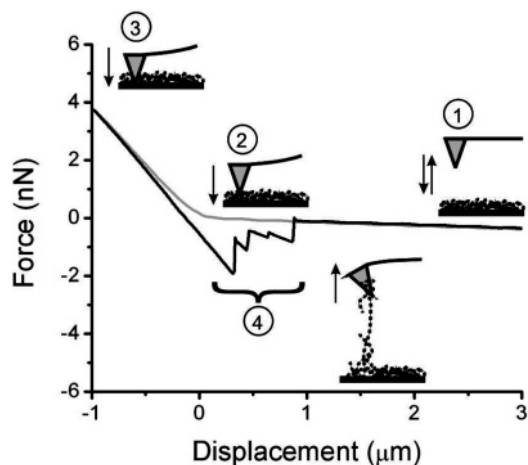
Figure 2.3 A typical force vs displacement curve recorded as the AFM tip approaches (gray line) and retracts (black line) from an aggregate-coated silicon substrate. The light gray curve represents the force acting on the tip as it moves toward the substrate surface (step 1), at the contact point (step 2), and while it is indented into the sample (step 3). The black line is the force acting on the tip as it moves away from the surface (step 4).

In this study, Bruker's Dimension Icon AFM at York center, New Jersey Institute of Technology, was used for ultrasensitive force detection to quantify the mechanical properties of the soot aggregates. Soot (240 nm mobility diameter) was collected on silicon substrate using electrostatic deposition. Then, AFM was used to do force-distance measurements.

CHAPTER 3

RESTRUCTURING OF SOOT UPON EXPOSURE TO INTERMEDIATE VOLATILITY CHEMICALS

3.1 Restructuring Caused by Capillary Condensation in Subsaturated Vapor

Major motivation of this study comes from the previous project of our research group (Chen et al., 2018), where soot particles of known size were exposed to vapors of different chemicals. Based on the size and mass measurements, all the coatings fall into two distinct groups based on their restructuring ability (Figure 3.1). For the chemicals in the red group, soot aggregates shrink gradually with an increase in coating mass. On the other hand, chemicals in blue group, induced a complete restructuring with a mass fraction as low as ~5%. In fact, these two groups have different volatilities. Chemicals in the blue group have intermediate volatility, such as triethylene glycol with vapor pressure of 0.18 Pa at 298 K, and chemicals in the red group are low volatile such as sulfuric acid with vapor pressure of 3.87×10^{-7} Pa. Two condensation mechanisms have been proposed; uniform condensation of the low volatile coatings, resulting in gradual restructuring, and condensation of the intermediate volatile coatings in small angle cavities of the soot aggregate (capillary condensation), that is more effective in restructuring for comparable coating mass. A complete restructuring with a mass fraction as low as ~5% raised the question of whether it is possible that coating is lost before mass/size measurements for the case of blue group which are more volatile, leading to mass of the coating underestimated. To answer this question, a study was performed using chemicals of blue group as condensable vapor on the soot aggregates.
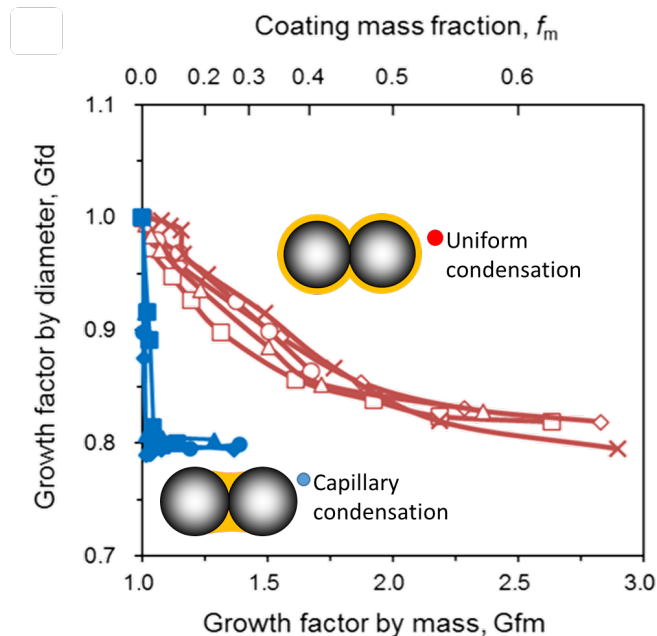
Figure 3.1 Morphological changes occurring in soot aggregates that were exposed to condensable vapors of different chemicals and then denuded.
Source: (Chen et al., 2018).

As described in Chapter 2, soot particles size selected by DMA1 were exposed to various levels of vapor supersaturation, which can be changed by the temperature of the chamber. After leaving the chamber, flow temperature decreases, and condensation occurs on particles. Then changes in size and mass of the particles were measured. Considering the position of our sizing instrument, DMA2, which was far from the coating chamber, and because of the sheath flow in DMA, particles might lose coatings by evaporation. So, to measure the size of the particles before reaching our typical sizing instrument (DMA2), we built a small electrostatic classifier (EC) (Figure 3.2) that was easy to move, can be placed at certain distances from the coating chamber to measure the size of the particles (Figure 3.3). The EC works based on the principle similar to DMA, but unlike DMA, there was no sheath flow in EC to cause evaporation of the coatings. The EC is connected to high voltage, and based on the electrical mobility of the particles, they passed through or become

collected on the rod, with the applied voltage proportional to the diameter of classified particles.
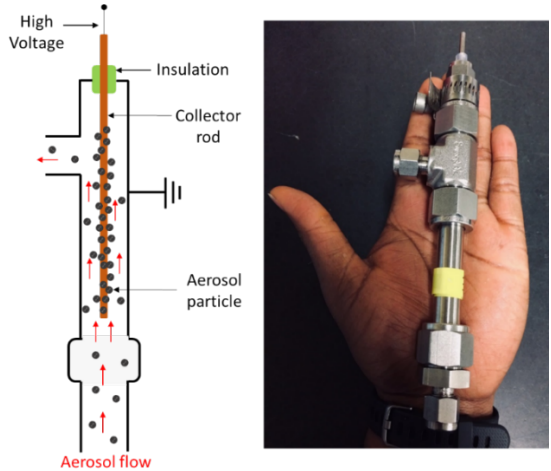
Figure 3.2 Schematic of the EC (left), real EC (right).
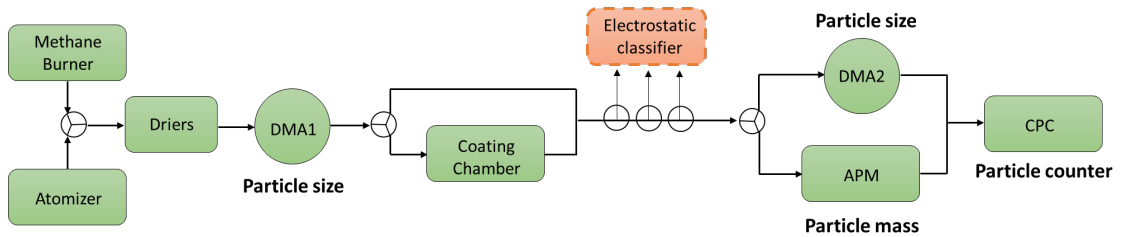
Figure 3.3 Schematic of the system for aerosol generation, processing and analysis + Electrostatic classifier.

To use the EC, the relationship between applied voltage and mobility diameter of particles must be known. Accordingly, we used particles of known size to determine the voltage corresponding to a certain transmission efficiency. We used 50% collection efficiency (Figure 3.4a). The derived plot was used to determine the diameter of the particles which have 50% collection at a specific voltage (Figure 3.4b).
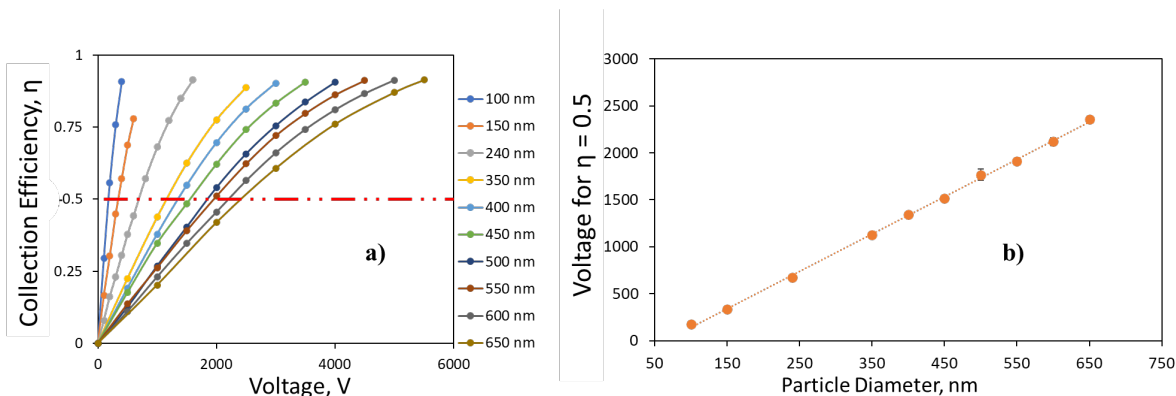
Figure 3.4 (a) collection efficiency vs voltage for particles of known size, and (b) calibration plot to determine the diameter of the particles which have 50% collection at a specific voltage.

Soot particles were sent to the coating chamber, including triethylene glycol (TEG), one of the chemicals of the blue group which has intermediate volatility. By increasing the temperature of the coating chamber, the amount of condensate increased, resulted in particle growth. This growth was measured by our sizing tools, EC which was placed after the coating chamber and DMA2 which was far away. The growth factor by diameter versus temperature of the coating chamber is plotted in Figure 3.5 for both EC and DMA2 measurements. As shown in this plot it is obvious that the amount of the condensate was underestimated by our research group for the intermediate volatility chemicals (Chen et al., 2018). The EC, which was after the coating chamber, showed size increase owing to growth and encapsulation, while DMA2 showed compact aggregate because of evaporation of the condensate before reaching DMA2.
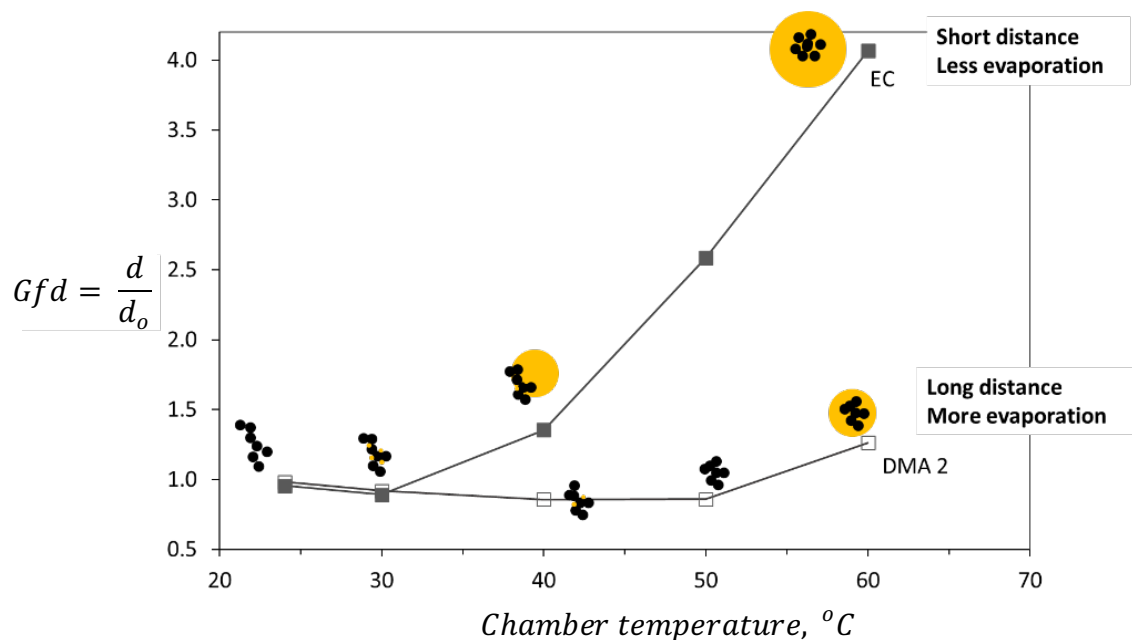
Figure 3.5 The growth factor by diameter versus temperature of the coating chamber including TEG.

As shown in Figure 3.6, using fractal soot (240 nm) and its volume equivalent spherical particles (150 nm PSL, has the same volume as a 240 nm fractal particle) near room temperature, there is not any growth for spherical particles. Because of the Kelvin effect, the vapor pressure of the convex surface of droplet is greater than saturated vapor pressure of TEG. So, there is no condensation and growth. On the other hand, for fractal particles there is capillary condensation between the junctions of the monomers because the vapor pressure above the concave surface is less than saturated vapor pressure. This capillary condensation leads to partial restructuring, which can be seen better by zooming in to relative growth in diameter near room temperature (see inset). At room temperature the size of the spherical particle does not change, but there is soot shrinkage that increases by increasing the temperature. Both EC and DMA2 measurements show similar shrinkage for soot aggregate, implying that there is not any growth and encapsulation near room

temperature. So, restructuring occurs as a result of the capillary condensation. Increasing the temperature leads to higher supersaturation, and condensation can encapsulate the entire aggregate and grow the droplet to large sizes. When soot aggregate gets fully encapsulated, it behaves as its volume equivalent spherical particle, and points for fractal and spherical particles merge.
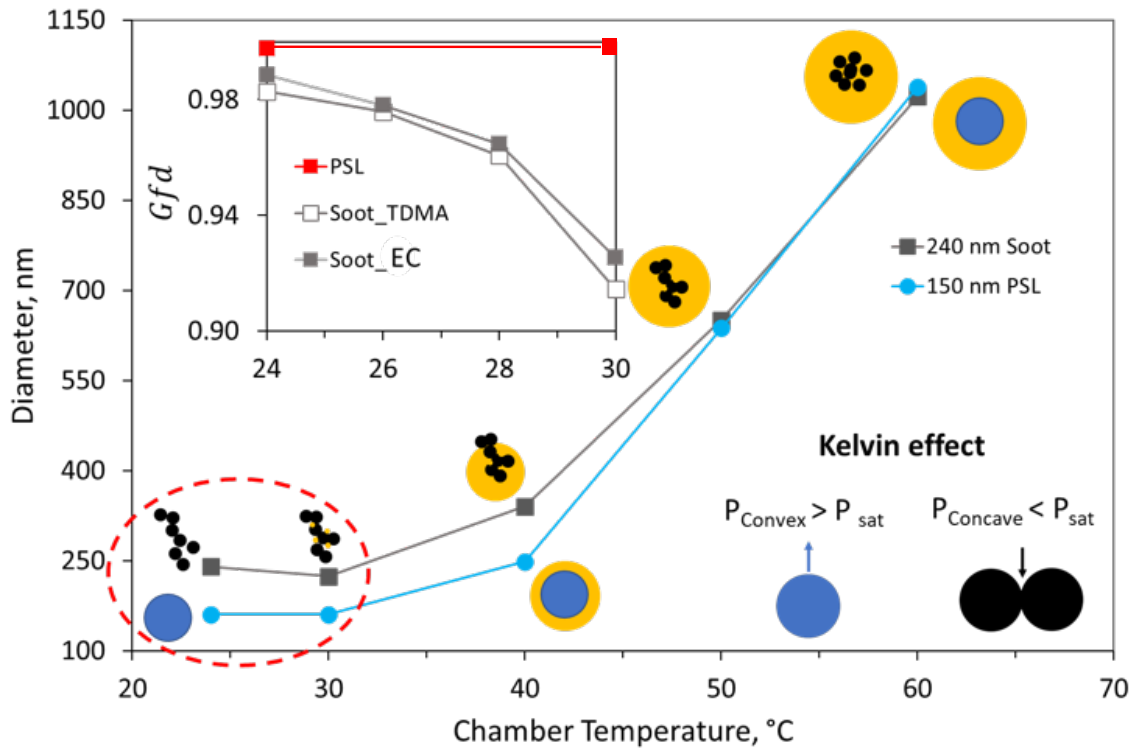
Figure 3.6 Soot restructuring caused by capillary condensation in subsaturated vapor of TEG and particles encapsulation in higher supersaturations.

3.2 Separating Restructuring Caused by Condensation and Evaporation

Studies have shown that fractal aggregates restructure and become compact due to the presence of liquid coatings acquired via condensation (Pagels et al., 2009; Schnitzler et al., 2014). On the other hand, the results of the study by Ma et al. (2013) showed that restructuring occurred only during droplet evaporation for water-coated aggregates. A

recent study by Bhandari et al. (2019) on cloud-processed soot aerosol also implied the occurrence of aggregate restructuring only after water evaporation, not during condensation. Based on the current literature, the relative roles of condensation and evaporation on aggregate restructuring are still not well established. So far, the conclusions made are due to the use of different types of soot, condensing vapors, saturation conditions, and processing methods. Because soot particles in the atmosphere can undergo both vapor condensation and evaporation, it is important to understand how each of these two processes affects the evolution of soot structure for better quantification of its environmental impacts.

We present the experimental measurements, elucidating the effect of condensation and evaporation on aggregate restructuring for a single type of soot exposed to water, a nonwetting liquid, and wetting liquids. To separate the role of the condensation and evaporation on soot restructuring, one must compare the structure of soot aggregates within droplet and after droplet evaporation. This can be achieved by measuring angular scattering of airborne aggregates or aggregates transferred into bulk liquid (Ma et al., 2013). We used a different approach, which is based on anchoring soot aggregates on a flat surface. In a recent study on the impact of sampling medium on particle morphology, by collecting soot aggregates on a flat surface like silicon chips, it was possible to anchor them (Chen et al., 2017) (Figure 3.7). Accordingly, in some of our experiments the coated soot particles were anchored by collecting them on silicon chips, before the particles could lose any coating material (1-2-5). In other experiments soot particles were allowed to lose all of the coating while airborne and only then they were collected on chips (1-2-3-6). The morphology of the particles collected in both ways was characterized based on convexity determined from

SEM images (Bhandari et al., 2019; China et al., 2013). Figure 3.7 includes scanning electron microscopy images of untreated fractal aggregates (7) and aggregates that were encapsulated and then lost their condensate while airborne (9) or after anchoring on silicon wafers (8). Morphology is characterized using convexity calculate from images.
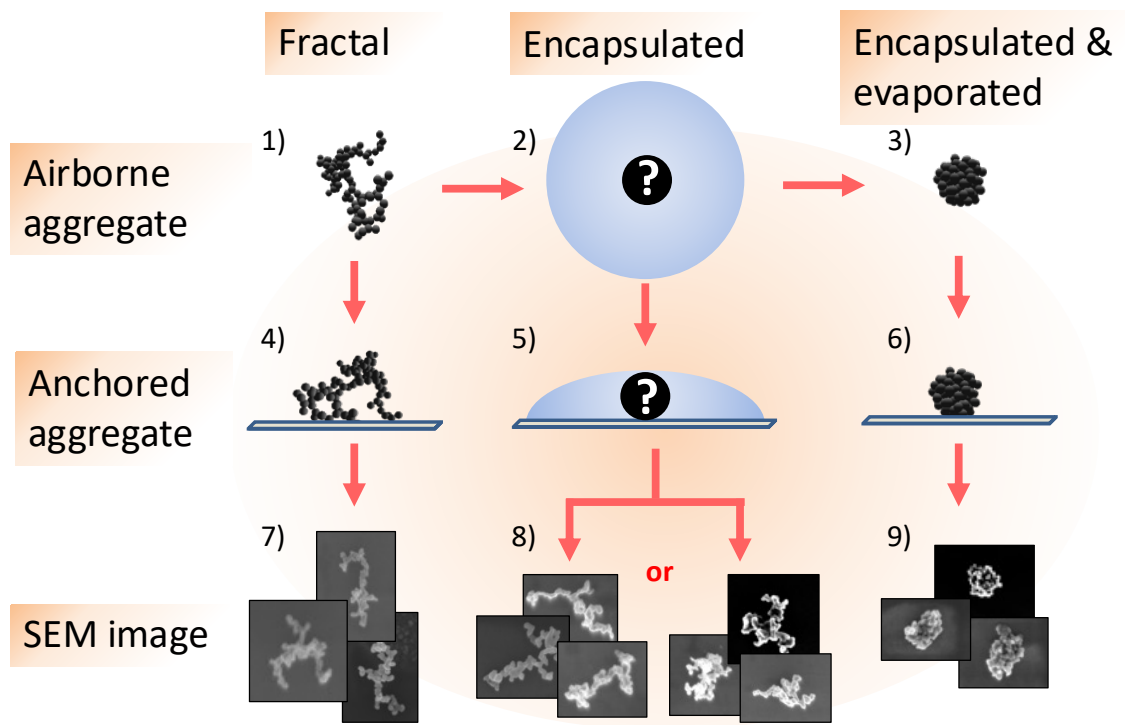
Figure 3.7 Separating the effect of the condensation and evaporation on soot restructuring by anchoring the aggregates on silicon wafers while encapsulated. Scanning electron microscopy images of untreated fractal aggregates, anchored aggregates while encapsulated and aggregates that lost their condensate while airborne.

Like in the previous section, to obtain coated particles, size-classified soot aerosol was passed through a saturator partially filled with a wetting liquid, triethylene glycol (TEG) and a non-wetting liquid, water. The temperature of the saturator was varied from ambient (~24 °C) to 60 °C to control p_{sat}. Upon exiting the saturator, vapor condensed on the soot particles and the change in particle mobility diameter was measured by EC after

droplet formation by condensation and then after droplet evaporation. The results of our particle size measurements immediately after encapsulation of soot aggregates and after coating evaporation are expressed in terms of diameter growth factor (Figure 3.8). The convexity of the aggregates was calculated using SEM images of the particles collected after condensation and then after evaporation (Figure 3.9).

With non-wetting water, particle size measurements (Figure 3.8a) show neither growth nor shrinkage of the soot aggregates by increasing the temperature of the saturator from ambient to 50 °C, because soot is hydrophobic and cannot be activated in low supersaturation (Ma et al., 2013; Zuberi et al., 2005). At 60 °C, measurement after condensation shows soot activation up to growth factor of 3.96. Growth factor after coating evaporation decreases to 0.8 due to restructuring of the soot aggregate. Since for an uncoated aggregate, particle mobility is unchanged (growth factor =1), a decrease in the particle mobility diameter is due to restructuring of the soot and an increase is due to addition of condensed coating (Enekwizu et al., 2021).

Figure 3.9a compares convexities of the soot particles that lost coating while anchored vs airborne. With non-wetting water, convexity of the airborne particles does not change (0.53) until 60 °C. A sharp increase in convexity of the airborne particles to 0.87 at 60 °C reveals that soot restructures by evaporation of the water (Ma et al., 2013), during shrinking of the evaporating droplet. However, convexity of the anchored soot does not change even after encapsulation at 60 °C, showing that soot remains fractal after water vapor condensation (0.53 is the convexity of the fractal aggregate). This happens because even when a droplet forms, water does not penetrate between the monomers in the soot aggregate and those gaps remain empty (Figure 3.10a). Since soot is hydrophobic and

fractal, it can be considered as a superhydrophobic surface for water with a large contact angle (>150°) (Onda et al., 1996). Molecular dynamics simulations show that holding water inside a 1.5 nm slit graphite pore requires 3500 atm pressure (Pršlja et al., 2019), which is much higher than the 1.4 atm Laplace pressure for a ~ 1 µm water droplet in our experiments.

For TEG, both EC and DMA measurements yield similar growth factor for soot at low saturator temperatures ($T \leq 30$ °C) but diverge for temperatures above 30 °C (Figure 3.8b). With the condensation curve, the saturator temperature increase above 30 °C causes a rapid growth to 4.1 at 60 °C, indicating the addition of a significant amount of condensate on the soot aggregates. With the condensation-evaporation curve, growth factor starts at 0.98 at ambient temperature, passes through a minimum (0.86) at 40 °C.
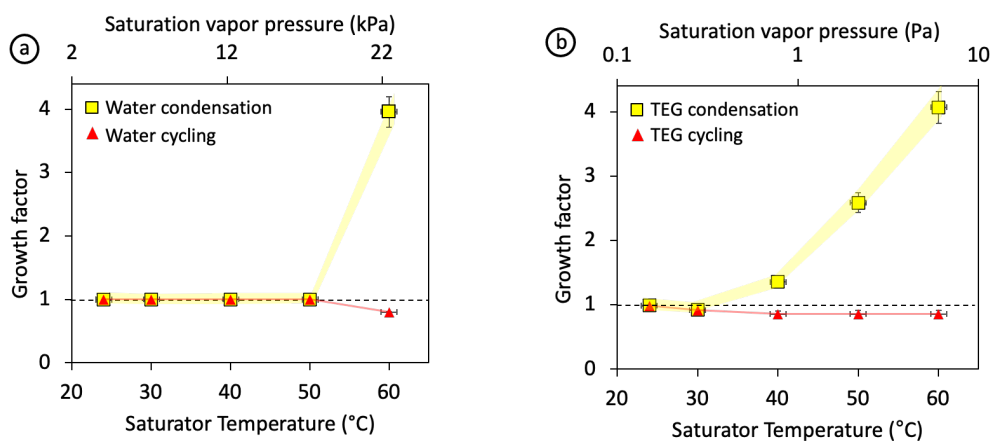
Figure 3.8 Bare soot aggregates subjected to a condensation-evaporation cycle with (a) water and (b) triethylene glycol: Particle growth factor measured immediately after encapsulation of airborne soot aggregates (yellow) and after coating shell evaporation (red).

Figure 3.9b shows that by increasing the supersaturation, convexity of the anchored soot increases from 0.53 to 0.73 at 30 °C, showing partial restructuring of the aggregates.

This happens because TEG is a wetting liquid, and its condensation occurs in junctions between the monomers and causes some restructuring (Enekwizu et al., 2021). At higher supersaturations (T ≥ 30 °C), the amount of condensate increases, and soot becomes encapsulated, causing more restructuring and convexity increases to 0.74. Considering soot particles that lost condensate while airborne, up to 30 °C, coating evaporation slightly increases convexity to 0.75. However, at higher supersaturations, evaporation of the coating causes full restructuring of soot, increasing the convexity to 0.88 (Figure 3.10b).
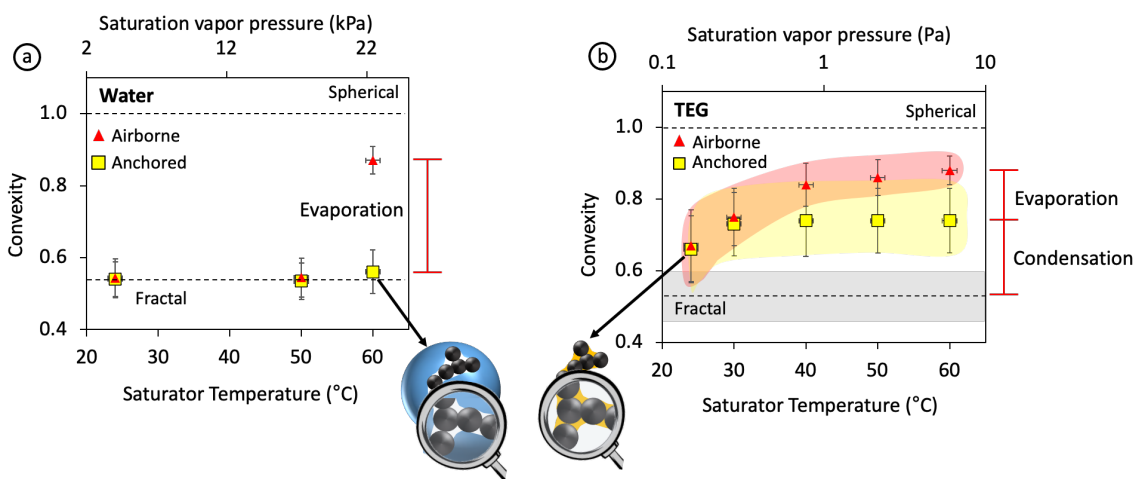
Figure 3.9 Bare soot aggregates subjected to a condensation-evaporation cycle with (a) water vapor and (b) triethylene glycol (TEG). Convexity corresponds to encapsulated soot aggregates that lost their condensate either while airborne or after anchoring on silicon wafers.
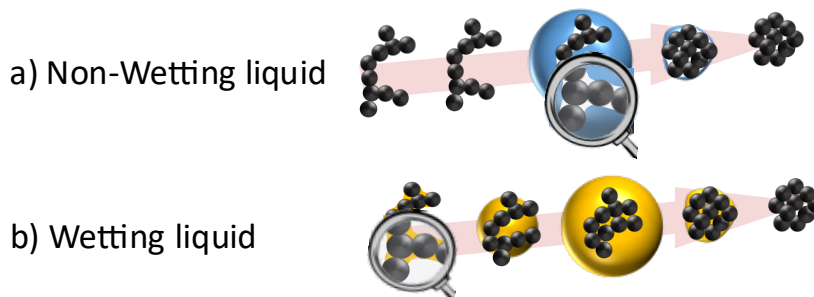
Figure 3.10 Soot aggregates restructuring by non-wetting and wetting liquids.

To conclude this chapter, wetting and non-wetting liquids act differently in soot restructuring. For the liquids capable of wetting the surface of soot aggregates, minor restructuring begins already during capillary condensation and significant restructuring occurs as the coating volume increases. With non-wetting liquids, such as water, it is the evaporation that drives most of restructuring and there is almost no restructuring during condensation.

CHAPTER 4

INTERACTION OF THINLY COATED SOOT PARTICLES WITH WATER VAPOR

4.1 Subsaturated Water Vapor

In this project, the role of the subsaturated water vapor in restructuring of lightly coated (<10% by mass) soot particles was investigated. Because soot particles are hydrophobic and require high water supersaturations to be activated, they typically exhibit little structural or morphological difference between dry and saturated relative humidity (RH) conditions. However, hydrophilic soot particles produced by condensation of water-soluble compounds, takeup water at elevated relative humidity (10-85%) and their total volume increases sufficiently (e.g., by a factor of 2-4) to promote restructuring and collapse into globules (Zhang et al., 2008). Previously the effect of relative humidity on restructuring of soot coated with different chemicals such as sulfuric acid, dicarboxylic acids, and ammonium nitrate has been shown (Khalizov et al., 2009; Xue et al., 2009; Yuan et al., 2020). In a recent field study it has been found that the morphological restructuring of the soot aggregates is associated with coating and relative humidity (Xu et al., 2020). Most recent study has suggested that high relative humidity contributes to a thicker coating of nitrate on black carbon particles, resulting in restructuring and optical properties enhancement (Zhou et al., 2022). So far, studies on the effect of humidity on the restructuring behavior of coated soot have been done with thickly coated soot (Khalizov et al., 2009; Xue et al., 2009; Yuan et al., 2020).

In the atmosphere, soot is subject to aging through the condensation of different chemicals (China et al., 2015). Condensate (coating) can be distributed uniformly over the

monomer spheres comprising the aggregate or instead reside in junctions between the monomers, depending on the vapor supersaturation (Equation 4.1) of the condensing chemicals. At high supersaturations, vapor condenses uniformly over aggregates, including convex monomers and concave junctions in between monomers, but with low supersaturations, junctions become preferred. (Chen et al., 2018; Ivanova et al., 2020).

$$\zeta = \left(\frac{P}{P_{sat}}\right) - 1 \qquad (4.1)$$

Our motivation was to investigate the restructuring of soot aggregates primed with a small amount of water-soluble material delivered by capillary condensation at $\zeta < 0$ and then exposed to an increased relative humidity. We were motivated by field and cloud chamber observations of compact but uncoated soot particles (Bhandari et al., 2019). In the field studies (China et al., 2015), soot compaction has been attributed to cloud activation of soot aggregates followed by droplet evaporation (Ma et al., 2013). However, our hypothesis is that even without cloud activation, soot lightly coated with hygroscopic chemicals may become compact upon moderate humidification (10-85% RH). In the experiments, we first applied light coats of hygroscopic chemicals on soot, using capillary condensation. The amount of condensate was less than 2-3% by mass. Then we quantified the change in morphology of the coated soot aggregates after exposure to elevated relative humidity (10-85%).

Aerosol Coating and Humidification Experiments

Size classified particles (240 nm mobility diameter) were passed through a reservoir partly filled with a coating material (Figure 3.3). The reservoir was maintained at room temperature (24°C) to have thinly coated soot aggregates. The coating materials used in

our experiments and their properties are listed in Table 4.1. After passing soot particles through a Nafion humidifier, by using hygroscopicity tandem differential mobility analyzer (H-TDMA), we determined the mobility diameter of the coated soot aggregates before and after exposure to elevated relative humidity (10-85%). Changes in particle size are reported in terms of diameter growth factor. The relative error in the H-TDMA measurements was less than 1%.

Table 4.1 Properties of the Coatings

Coating material	Acronym	CAS #	Mw[a], g mol^{-1}	ρ[b], g cm^{-3}
Triethylene glycol	TEG	112-27-6	150.17	1.12
Triethylene glycol monobutyl ether	TEGMBE	143-22-6	206.28	0.99
Ammonium nitrate	AN	6484-52-2	80.04	1.72
Glutaric acid	GA	110-94-1	132.12	1.3
Sulfuric acid (H_2SO_4, 78 wt %)	SA	7664-93-9	98.08	1.60

Table 4.1 Properties of the Coatings

Coating material	P_{sat}[c] at 25 °C, Pa	γ[d], mN m^{-1}	K[e], nm	Gfv[f]
Triethylene glycol	0.18	46.5	5.0	1.6
Triethylene glycol monobutyl ether	0.33	31.4	5.3	1.6
Ammonium nitrate	1.33×10^{-3}	72	2.7	4.0
Glutaric acid	6.7×10^{-4}	50	4.5	2.0
Sulfuric acid (H_2SO_4, 78 wt %)	3.16×10^{-6}	73	3.6	4.1

References to (a) molecular weight, (b) density, (c) saturated vapor pressure, (d) surface tension and (e) Kelvin length data sources: TEG (Yaws, 1998), TEGMBE (Boatman & Knaak, 2001), AN (Dionne et al., 1986; Yuan et al., 2020), GA (Bilde et al., 2003; Xue et al., 2009), SA (Daubert, 1989; Young & Grinstead, 1949). Hygroscopic growth factor by volume at 85%RH (f) calculated using data from : SA (Green & Perry, 2008; Tang, 1996), AN (Wu et al., 2019), TEG and TEGMBE (Guide), GA (Wise et al., 2003).

Modeling of the Vapor Supersaturation in the Saturator

An undergraduate researcher, Egor Demidov, performed the modeling of the vapor

supersaturation in the saturator. The flow was saturated with coating material vapors by

passing it through a chamber partially filled with liquid coating material at room

temperature. As the flow progressed through the saturator, vapor diffused from the liquid

surface into the flow. Vapor concentration at each point in the flow at steady state can be

found by solving Equation (4.2), where $\vec{v}$ is flow velocity vector, c is vapor concentration,

and D_i is diffusivity of the coating material in air. Geometry of the saturator was not

cylindrical, as it was partially filled with the coating material. Hence, the Navier-Stokes

equation was solved using COMSOL to obtain the laminar flow profile within the saturator.

With the flow profile, Equation (4.2) could be solved with the finite element method.

$$\vec{v} \cdot \nabla c = D_i \nabla^2 c \qquad (4.2)$$

Two cases with different boundary conditions were considered to get a range of

possible solutions. In all cases, vapor concentration at the inlet was assumed to be zero

$c(x, y, 0) = 0$. Concentration near the vapor-liquid interface was assumed to be saturated

vapor at room temperature $c(x, 0, z) = c_{sat}$. Saturated vapor pressure at room temperature

was calculated with the Antoine Equation and related to vapor concentration through the

ideal gas law (Equation 4.3).

$$c_{sat} = \frac{p_{sat}}{RT} \qquad (4.3)$$

The boundary condition on the saturator wall was varied between trials. In case A, the wall

was set as a no-flux boundary. Physically, this means that the rate of vaporization from the

wall is equal to the rate of condensation onto the wall and the total amount of matter in the

vapor phase remains unaffected by the wall. This solution gave us the upper bound estimate of saturation ratio, as all vaporized material had to stay in the vapor phase. In case B, the concentration at the wall was set to zero. This means that that the wall was assumed to be completely dry. This way the wall acted as a sink for vapor and the solution provided the lower bound estimate for saturation ratio. After the solutions to Equation (4.2) were obtained at each point within the finite element mesh, mean concentration at different axial positions z needed to be found. The average value can be found by integrating the data numerically at a cross-sectional slice over the surface and dividing the result by cross-sectional area (Equation 4.4).

$$c_{mean} = \frac{\iint_S c(x,y,z)dS}{\iint_S dS} \tag{4.4}$$

Then saturation ratio is merely the ratio of mean concentration to saturated vapor concentration at room temperature (Equation 4.5).

$$SR = \zeta + 1 = \frac{C_{mean}}{C_{sat}} \tag{4.5}$$

Calculation of the Condensation Rate

The vapor condensation rate on a sphere has been well established under free-molecular, continuum, and transition regimes by Seinfeld and Pandis (1998). A graduate researcher, Ella Ivanova modified the condensation rate equation for free-molecular regime (Equation 4.6), considering two cases of condensation: formation of a uniform film on the surface of the spheres and capillary condensation, filling the gap between the spheres (Figure 4.1) (Ivanova et al., 2020).
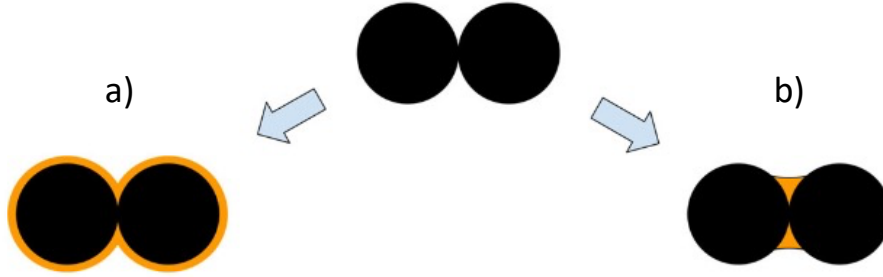
Figure 4.1 Two cases of condensation, (a) formation of a uniform film on the surface of the spheres, and (b) capillary condensation, filling the gap between the spheres.

The modified Equation (4.6) shows the change in the volume of the condensate with time, using dimensionless variables (Equations 4.7 – 4.10), where R_s is the monomer sphere radius, ℓ_K is the characteristic Kelvin length, $\tilde{V}$, $\tilde{A}$, and $\tilde{\kappa}$ are the dimensionless volume, area, and curvature of a spherical shell or the gap in the junctions between monomers, respectively. With the $\tilde{t}$, dimensionless time, α is the molecular accommodation coefficient, v_T is the mean thermal velocity of the molecules, n_0 is the unperturbed vapor number density far from the droplet, and n_l is the number density of the liquid phase. In characteristic Kelvin length (Equation 4.11), γ is the vapor-liquid surface tension, V_m is the molar volume, R_g is the gas constant and T is the temperature.

$$\frac{d\tilde{V}}{d\tilde{t}} = \tilde{A}\left(1 - \frac{1}{\zeta + 1}\exp\left[\frac{\ell_K \tilde{\kappa}}{2R_s}\right]\right) \tag{4.6}$$

Dimensionless variables:

$$V = \tilde{V} \cdot R_s{}^3 \tag{4.7}$$

$$A = \tilde{A} \cdot R_s{}^2 \tag{4.8}$$

$$\kappa = \tilde{\kappa} \cdot R_\text{s}^{-1} \tag{4.9}$$

$$t = \tilde{t} \cdot \frac{4 \, n_\text{l} R_\text{s}}{\alpha v_\text{T} n_0} \tag{4.10}$$

$$\ell_\text{K} = \frac{2\gamma V_\text{m}}{R_\text{g} T} \tag{4.11}$$

The condensate volume can be considered a function of filling angle for gap (Figure 4.2a).

We assumed a 10 degrees carbon neck angle when modeling the condensation.

$$\frac{d\tilde{V}}{d\tilde{t}} = \frac{d\tilde{V}}{d\theta} \frac{d\theta}{d\tilde{t}} \tag{4.12}$$

For the condensation on the sphere, the volume can be considered as a function of the

change in the condensate layer on the surface of the sphere ($\tilde{R}$) (Figure 4.2b).

$$\frac{d\tilde{V}}{d\tilde{R}} = \frac{d\tilde{V}}{d\tilde{R}} \frac{d\tilde{R}}{d\tilde{t}} \tag{4.13}$$
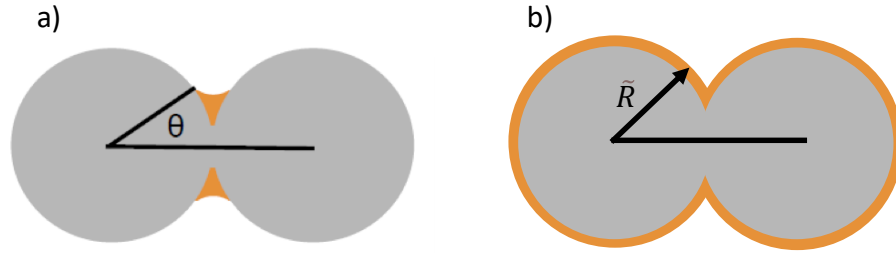
Figure 4.2 Filling angle θ of the condensate in the gap between the spheres.

The sulfuric acid (SA) in this study is 78% wt. solution, with H_2SO_4 saturation

vapor pressure of 3.16E-06 Pa. However, the composition of SA on the surface of the

particles is 70.6% in equilibrium with 5% RH of the sample flow, corresponding to SA

saturation vapor pressure (p_{sat} = 2.38E-07 Pa) (Taleb et al., 1996). Therefore, SA saturation ratio is greater than unity (13.3), condensation occurs both in the gap and on the surface of monomers (Chen et al., 2018; Ivanova et al., 2020). Glutaric acid (GA) and ammonium nitrate (AN) in coating reservoir are solid, but on the surface of the particles they condense as liquids (Ma et al., 2017; Xue et al., 2009). Saturation vapor pressure of the solid GA is (2.5E-04 Pa), less than its liquid phase (9.2E-04 Pa) (Bilde et al., 2003). So, GA saturation ratio is less than unity (0.27), condensation occurs only in the gap between the monomers. Saturation vapor pressure of the solid AN is (1.2E-03 Pa), less than its liquid phase (2.9E-03 Pa) (Tang, 1996). So, saturation ratio of AN is less than unity (0.42), condensation occurs only in the gap between the monomers. Triethylene glycol (TEG) and triethylene glycol monobutyl ether (TEGMBE) are liquid in coating reservoir and on the surface of the particles condense as a liquid too. At room temperature, saturation ratio of TEG and TEGMBE is less than unity, 0.65, condensation occurs only in the gap between the monomers.

Restructuring Experiments

In the experiments, soot particles were made lightly coated by sending them through a coating reservoir with the selected material at room temperature. Then we quantified the change in morphology of the coated soot aggregates before and after exposure to elevated relative humidity. According to the APM measurements, the mass of the soot aggregates did not change after exposure to condensable vapors because the coating mass was below the detection limit of the APM (2-3%). Changes in the growth factor of the soot aggregates upon exposure to subsaturated water vapor are illustrated in Figure 4.3a. Uncoated soot did not show changes in the entire RH range. There is no observable change in the structure of

thinly coated soot with ammonium nitrate, sulfuric acid and glutaric acid at 5% RH. With

TEG and TEGMBE, intermediate volatile chemicals, aggregates undergo a minor

restructuring, with a growth factor of 0.983 at 5% RH. However, these thinly coated soot

aggregates restructured significantly with an increase in RH. We found that studied

chemicals fall into two groups based on their response to humidification. With an increase

in relative humidity, soot aggregates coated with TEG and TEGMBE restructured more

significantly compared to soot coated with sulfuric acid, ammonium nitrate and glutaric

acid. For glutaric acid, soot restructuring happens only after reaching the glutaric acid

deliquescence point (83-89% RH). No change is observed when glutaric acid-coated

aggregates are exposed to elevated relative humidity below the point of deliquescence of

glutaric acid, similar to the study by (Xue et al., 2009).
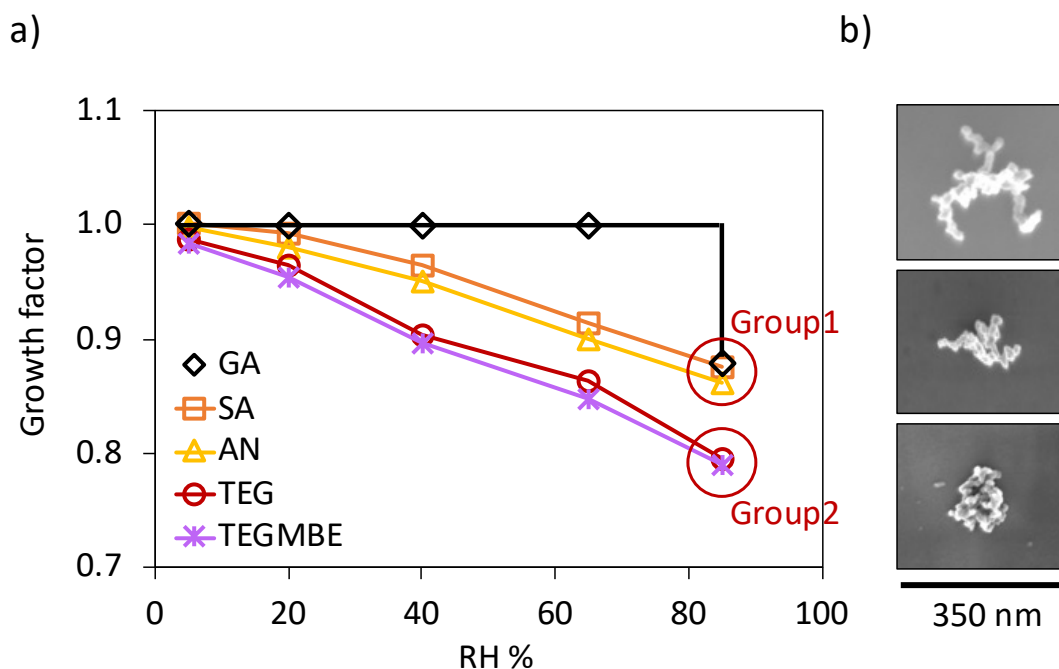
Figure 4.3 Particle growth factor measured as a function of relative humidity for lightly coated soot aggregates with sulfuric acid, TEG, TEGMBE, glutaric acid, and ammonium nitrate.

A significant restructuring also can be seen in scanning electron microscopy images in Figure 4.3b, in which fractal thinly coated soot aggregates became fully compact at 85% RH, with an increase in convexity from 0.53 (fractal) to 0.89 (compact). Since bare soot showed no change upon humidification, we can conclude that a small amount of condensate/adsorbate was formed on the particles, otherwise they would not have restructured. Because the coating mass was below the detection limit of the APM, we estimate that the amount of coating was less than 2-3% by mass, corresponding to a coating thickness of ~ 0.3 nm or a filling angle of < 35 degrees, for uniform and capillary condensation, respectively.

Soot aggregates lightly coated with TEG and TEGMBE restructured more in comparison to soot coated with GA and AN. This significant difference in the restructuring behavior may be related to the higher rate of condensation and higher supersaturation for TEG and TEGMBE compared to GA and AN over a fixed contact time, leading to a faster increase in the filling angle. SA, AN, and GA produce a lower filling angle because of the lower growth rate. SA has the least condensational growth rate among the coatings in this study. As a result, the amount of the SA condensed on soot aggregates is less than the other coatings. However, SA has the one highest hygroscopic growth factor by volume, leading to have a comparable restructuring behavior to soot coated with AN and GA.

Estimation of the condensate mass on soot particles

The two solutions for modeling of the TEG vapor supersaturation in the saturator were plotted as a function of axial position z (Figure 4.4). Case A showed that saturation ratio of 0.90 could be attained. Case B converged at 0.35. Overall, the range of possible values can lie anywhere between 0.35 and 0.90 based on the condition of the wall. So, with the

TEG, TEGMBE, GA, and AN that the saturation ratio is between 0.35 and 0.9 (Figure 4.4), capillary condensation occurs into the junctions between primary spheres in aggregates (Chen et al., 2018; Enekwizu et al., 2021; Ivanova et al., 2020). Within the range of saturation ratio (0.35 - 0.9), we considered 0.65 and calculated filling angle versus time in the coating reservoir (Figure 4.5). For SA as discussed before, saturation ratio is greater than unity (13.3), condensation occurs in the gap and on the surface of monomers.
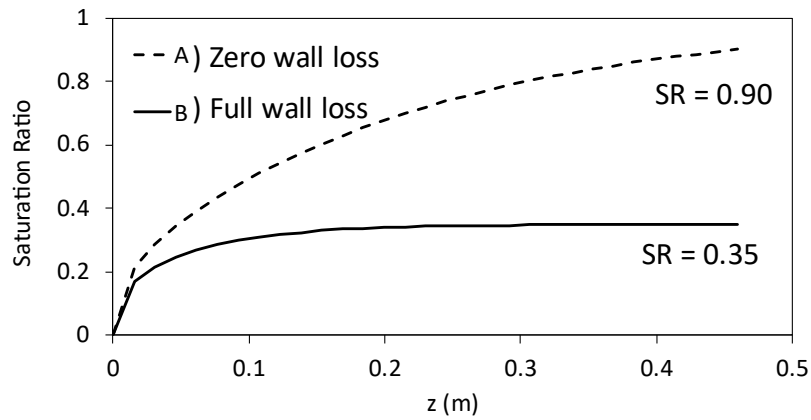
Figure 4.4 Average saturation ratio of TEG as a function of axial position. (a) zero flux at reactor wall, (b) zero vapor concentration at the wall.
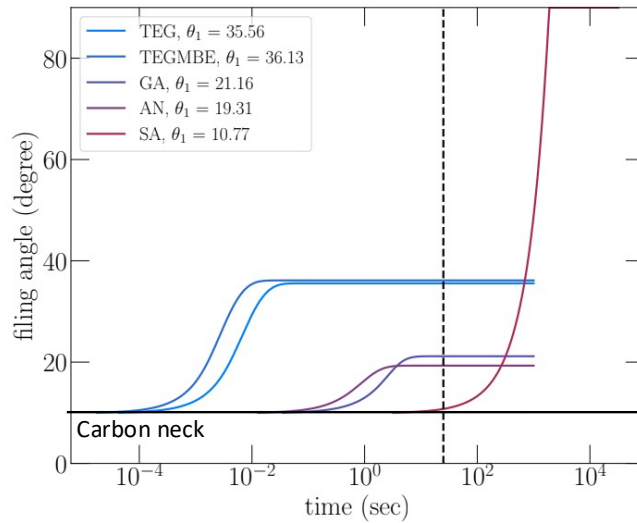
Figure 4.5 Filling angle of junctions between monomers for TEG, TEGMBE, AN, GA (saturation ratio = 0.65) and SA coatings (saturation ratio = 13.3). The dashed line shows the residence time of the soot aggregates in the coating reservoir.

From the curves of Figure 4.5 we obtained the maximum filling angle at the exit of the coating reservoir for different chemicals. Using these filling angles, the model solves Equations (4.6), (4.12), and (4.13) to calculate the volume of the coating in the gap between monomers. To calculate the humidified volume of the coating, as a zero-order approximation, the coating volume of condensate at the exit of the coating reservoir can be multiplied by the volume growth factors at different RH. This approach gives small change in humidified volume because it is missing an important factor, curvature. We ended up using a more advanced approach, assuming that the droplet between two monomers has the form of a globoid with a curvature (Figure 4.6). (Ivanova et al., 2020). Thus, we consider that the Kelvin effect helps the condensation process while the filling angle is less than 56 degrees. Because for the filling angles greater than 56 degrees, curvature becomes positive (Figure 4.7), and globoid and catenoid condensation occurs only in saturation ratios greater than unity.
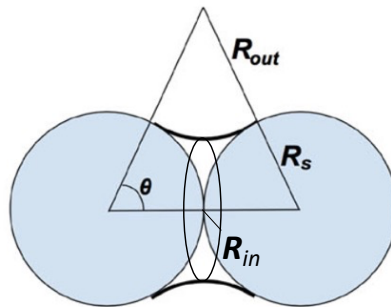
Figure 4.6 Two-dimensional projection of the droplet geometry considered in this work for condensation in the gap, with the nearly zero contact angle at the solid–liquid interface as a globoid.
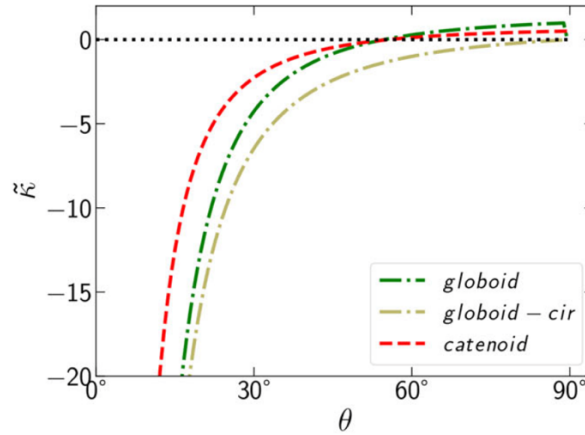
Figure 4.7 Condensate surface curvature $\tilde{\kappa}$ as a function of the filing angle.

Condensation of water is modeled using an iterative procedure. We add a small amount of water to the coating meniscus, which leads to an increase in the filling angle, $\delta\theta$. Further, we calculate the new aqueous meniscus composition and compare the vapor pressure of the water above the mixture and in humidifier. When water vapor pressure reaches water vapor pressure in humidifier, system is equilibrated, and the filling angle after the humidifier is obtained, θ_2 (Figure 4.8). The relative humidity versus θ_2 is plotted in Figure 4.9, showing increase in filling angle by increasing the relative humidity for all chemicals. SA, AN, and GA have less amount of condensate than TEG and TEGMBE at 5% RH. However, SA, AN, and GA have higher hygroscopicity (Table 4.1), leading to more water condensation and increase in filling angle only slightly below of that for TEG and TEGMBE at 85% RH.
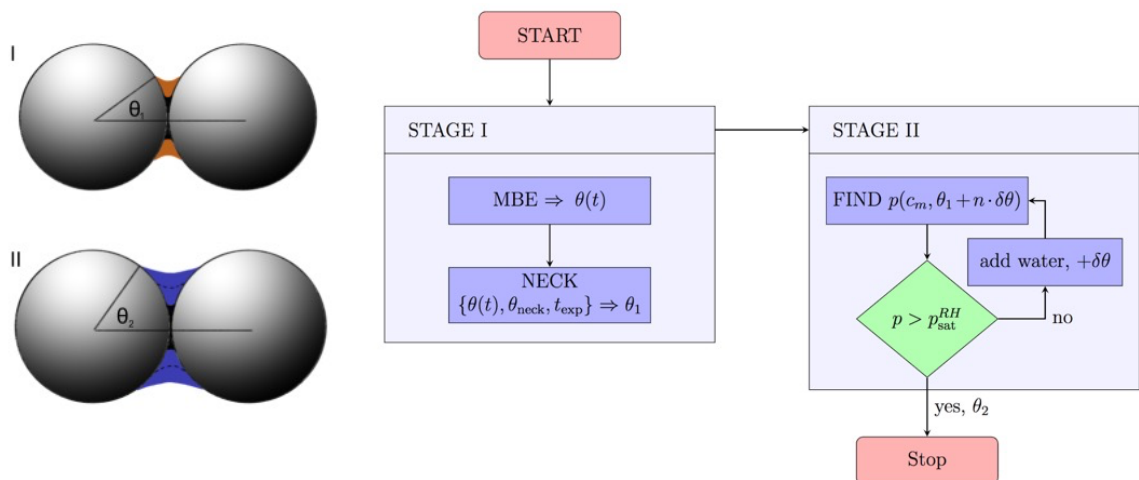
Figure 4.8 Schematic of the model that used to calculate the condensation of coating material (stage I) and water (stage II). (MBE: material balance equation).
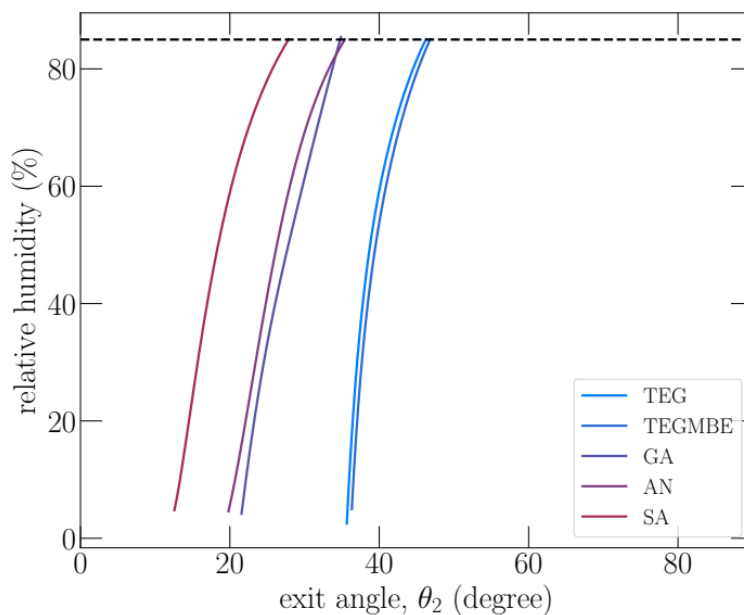
Figure 4.9 Relative humidity versus aqueous coating filling angle (θ_2) for TEG, TEGMBE, GA, AN, and SA.

Figure 4.10 is the experimental particle growth factor, showing shrinkage as a function of the calculated aqueous coating filling angle. Dioctyl sebacate (DOS) curve is experimental growth factor as a function of the pure coating filling angle from previous

study (Chen et al., 2018). Chemicals of the Group 1 have higher hygroscopicity in comparison with the chemicals of the Group 2, leading to more water condensation by increasing the RH%. However, the amount of the neat condensate for Group 1 was less than for the chemicals of the Group 2, leading to a larger humified filling angle and more restructuring by the chemicals of the Group 2. With the DOS, the neat coating filling angle should reach 60 degrees to have a comparable restructuring to the chemicals of the Group 1 with humidified filling angle < 40 degrees. This may be related to the higher surface tension of aqueous coating, resulting in more restructuring (Kütz & Schmidt-Ott, 1992).
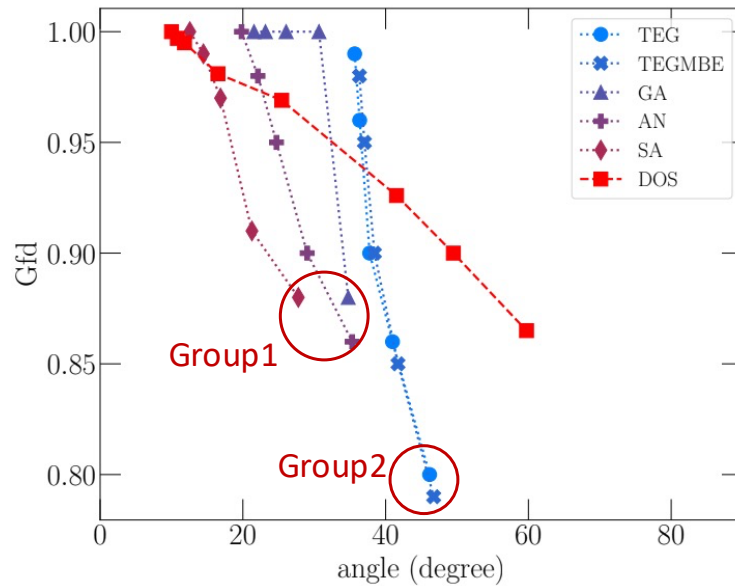
Figure 4.10 Particle growth factor as a function of the filling angle of the humidified coating.

4.2 Supersaturated Water Vapor and Cloud Processing of Soot Aggregates

In this section, the effect of the supersaturated water vapor on restructuring of the soot aggregates will be investigated. Soot particles in the atmosphere go through aging processes, in which they may get coated with water-soluble or water-insoluble chemicals. Then, these coated soot particles begin to serve as centers for water vapor condensation, leading to cloud droplet formation. By continuous cooling of the moist air, supersaturation increases ($\zeta > 0$), but then becomes depleted by the condensation on nuclei due to droplets growth. Exposing soot to supersaturated water vapor can lead to water uptake and restructuring (Zuberi et al., 2005). This restructuring of aged and processed soot after water condensation and evaporation has been observed by others (Mikhailov et al., 2001; Weingartner et al., 1995; Zuberi et al., 2005). However, a significant ambiguity is whether the restructuring occurs during the water uptake or during removal of water. Ebert et al. studied water uptake of ambient soot using E-SEM, but they could not see the aggregate before water evaporation and found soot to be more compacted after water evaporation (Ebert et al., 2002). In another study by Ma et al., restructuring of soot has been attributed to water evaporation (Ma et al., 2013). Köllensperger et al. using in-situ atomic force microscope investigated soot aerosols exposed to different humidities <100%, and found a decrease in particle size occuring during both water condensation and evaporation (Köllensperger et al., 1999), however, this observed effect was minor and inconclusive.

To determine the relative roles of the water vapor condensation and evaporation on restructuring of hydrophilic soot particles coated, size-classified soot aerosol was passed through the first saturator partially filled with hydrophilic material at ambient temperature, and then, through the second saturator filled with water. The temperature of the second

saturator was varied from ambient to 60 °C. Airborne soot particles were encapsulated by exposing them to supersaturated water vapor and then the coating was allowed to evaporate, while monitoring the particle size via electrical mobility measurements. Some of the coated airborne soot particles were anchored by collecting them on silicon chips, before the particles could lose any coating material. Other soot particles were allowed to lose all of the coating while airborne and only then they were collected on chips. The morphology of the particles collected in both ways was characterized based on convexity determined from SEM images. The reported convexity for each experimental point in this study is the average of the convexity of 100 soot particles.

We used two hydrophilic coating materials, SA and TEG. SA condenses uniformly on soot and makes the surface of the soot less hydrophobic (Chen et al., 2018). Convexity measurements, illustrated in Figure 4.11b (orange line), show that sulfuric acid alone causes no restructuring. However, it makes the surface of the soot less hydrophobic (Khalizov et al., 2009; Zuberi et al., 2005), resulting in restructuring by water condensation. From ambient temperature to 40 °C convexity increases from 0.64 to 0.8. By increasing the temperature above 40 °C soot becomes encapsulated and within such encapsulated aggregates capillary forces are absent, causing no further restructuring of the anchored soot (Enekwizu et al., 2021). With the airborne soot particles (collected after coating evaporation), their convexity is comparable to the anchored soot for the saturator temperature below 40 °C. On the other hand, at saturator temperatures ≥ 40 °C, convexity of airborne soot reaches 0.89, because under these conditions the aggregate becomes fully encapsulated in a water droplet, whose evaporation causes full restructuring.
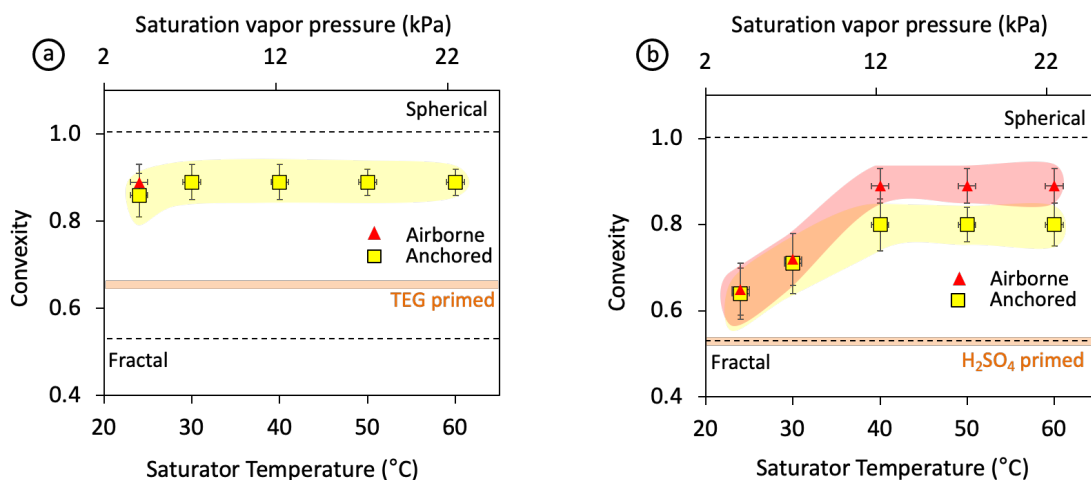
Figure 4.11 Triethylene glycol (TEG) and sulfuric acid primed soot aggregates subjected to a condensation-evaporation cycle with water vapor. Convexity of encapsulated soot aggregates that lost their condensate while airborne or after anchoring on silicon wafers.

Unlike SA, TEG condenses in the junctions between the monomers instead of condensing uniformly. TEG primed soot aerosol was sent to the second saturator filled with water. The temperature of the second saturator was varied from ambient to 60 °C. Based on convexity of the anchored particles, illustrated in Figure 4.11a, soot partially restructures already due to capillary condensation of TEG (Enekwizu et al., 2021) (convexity = 0.66, orange line). Then, TEG in the junctions between the monomers absorbs water at ambient temperature, swells in volume, leading to an increase in the filling angle of the aqueous menisci located in junctions, that becomes high enough to induce almost full restructuring (convexity = 0.86). A slight increase in convexity can be seen when soot particles were allowed to lose all of the coating while airborne (convexity = 0.89). By increasing the temperature of the water saturator, we see that anchored soot shows maximum compactness already at 30 °C upon water vapor condensation (convexity = 0.89).

We also quantified changes in soot morphology by measuring particle mobility diameter. According to the size measurements illustrated in Figure 4.12b, there is no restructuring caused by sulfuric acid (growth factor =1), because the amount of condensate was insufficient to induce any restructuring under dry conditions. However, soot particles primed with sulfuric acid uptake water at ambient temperature, restructure, and growth factor decreases to 0.96. Increasing the saturator temperature up to 30 °C leads to more water vapor condensation and restructuring, corresponding to the growth factor to 0.93. Both measurements, after condensation and after evaporation, yield similar growth factors for soot at low saturator temperatures ($T \leq 30$ °C), but diverge for temperatures above 30 °C. With the condensation curve, increasing the temperature to 60 °C leads to particle growth of 3.93 due to an addition of condensed water, leading to soot particles encapsulated in water droplets. If water is allowed to evaporate off encapsulated soot particles while they are airborne (condensation-evaporation curve), increasing the amount of the condensed coating produces an additional collapse of the aggregate. As the droplet continues to shrink, growth factor decreases to 0.8. For TEG (Figure 4.12a), there is some restructuring caused at ambient temperature due to capillary condensation (Enekwizu et al., 2021) (growth factor = 0.974). Both measurements, after water condensation and evaporation, yield similar growth factor for soot at low saturator temperatures ($T \leq 30$ °C), but diverge for temperatures above 30 °C. Like sulfuric acid, soot primed with TEG uptakes water at ambient temperature and leads to aggregate shrinkage (growth factor = 0.798). Because of being in the junctions, more restructuring occurs in comparison with the uniformly coated soot (Chen et al., 2016). By increasing the temperature of the second saturator to 30 °C, more shrinkage can be seen, because of more water vapor condensation, leading to a

decrease in the growth factor to 0.778. For temperatures above 30 °C, the condensation-evaporation curve reaches a minimum (0.777) at 40 °C, after which it remains flat. However, the condensation curve, shows particle growth to 4.06 due to addition of condensed water at 60 °C (Enekwizu et al., 2021).
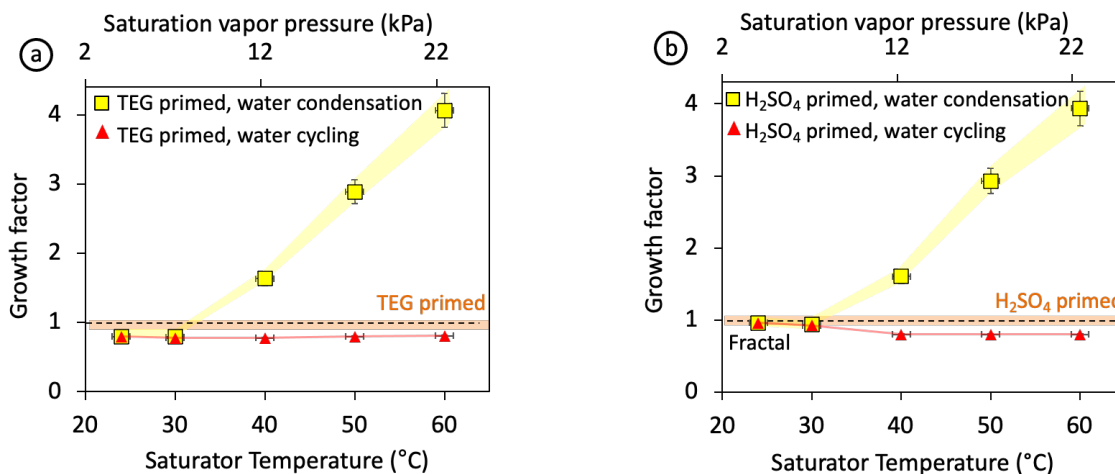
Figure 4.12 Primed soot aggregates with (a) TEG and (b) sulfuric acid, subjected to a condensation-evaporation cycle with water: Particle growth factor measured immediately after encapsulation of airborne soot aggregates (yellow) and after coating shell evaporation (red).

To conclude this chapter, soot can become fully encapsulated and restructured upon exposure to supersaturated water vapor (>100% RH), if the particles are primed with a monolayer of a hydrophilic chemical (TEG and SA). However, those primed soot particles restructure significantly even during exposure to subsaturated water vapor (<100% RH). Under subsaturated conditions, capillary condensation of hygroscopic chemicals can occur into the junctions between carbon spherules, driven by the saturation pressure depression caused by the concave menisci. Furthermore, the concave menisci promote absorption of a significant amount of water vapor by the condensate at moderate relative humidities, exceeding the amounts achievable for flat and convex surfaces. Exposure of fractal soot

particles to subsaturated vapors of hygroscopic chemicals in the atmosphere may be an important route towards soot compaction even at moderate relative humidities.

CHAPTER 5

MECHANICAL PROPERTIES OF SOOT AGGREGATES

The effect of soot on climate depends on its morphology, which can be changed from fractal to compact through the interaction with atmospheric chemicals. However, the mechanistic details of this restructuring remain poorly understood. In this study, AFM was used to quantify the mechanical properties of the bare fractal, thinly/thickly coated, and bare compact soot aggregates. Previously mechanical properties were studied only for bare nanoparticle chain aggregates (Rong et al., 2004). The experimental approach involved force-displacement measurements made with an AFM tip and an aggregate-coated substrate. Distinctive sawtooth patterns were observed which were interpreted as aggregate stretching and breaking events. Based on the measurements, estimates of the aggregate nanomechanical properties were made. Salameh et al. (2012) studied adhesion mechanisms of the contact interface of TiO_2 nanoparticles in films made of aggregates, demonstrating that information about the characteristic adhesion forces between individual monomers can be obtained experimentally, by means of AFM force measurements performed on freshly deposited particle films directly after flame spray pyrolysis synthesis. The employed strategy, repeated approaching/retracting loops of an AFM tip into the film, is capable of sensing primary particle/particle contact forces without specific functionalization of the tips with individual particles, which would be exceedingly difficult for particle sizes of few nanometers (Salameh et al., 2012).

In this study we used AFM to perform force-distance measurements. First, the sample is mapped to determine the locations of deposited soot aggregates (Figure 5.1a).

Also, 3-D image of a single soot aggregate can be obtained (Figure 5.1b). Next, the AFM tip is brought into contact with an aggregate on the surface of the substrate. Aggregate binds to the AFM tip (Figure 5.2). When the tip is raised, the attached spherules are pulled up and away from the aggregate deposited on the substrate. The force curve was determined by measuring the deflection of the cantilever as it approached and was retracted from the sample. During the retraction of the tip, the aggregate unfolds and ruptures leading to multiple peaks in each measured force−distance curve.
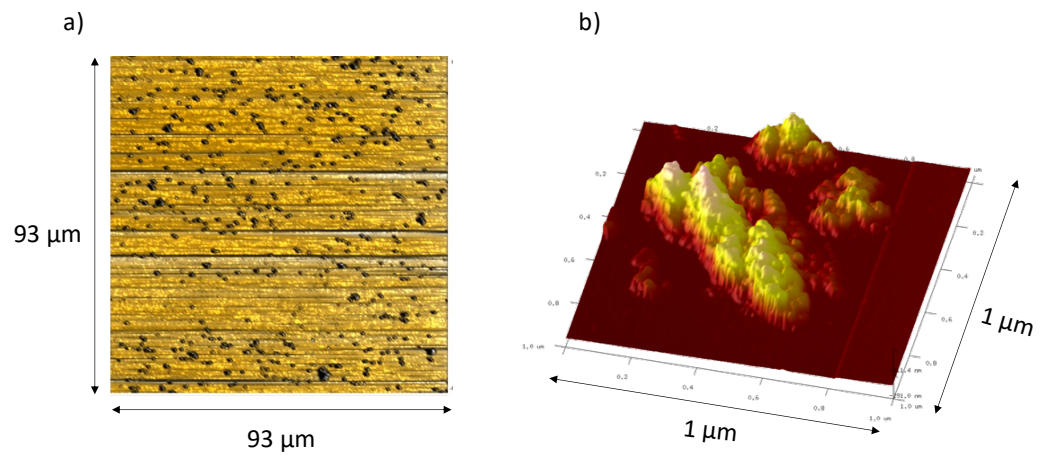
Figure 5.1 AFM images of bare fractal soot aggregate, collected on silicon chip. (a) Broad range scan to determine the locations of deposited soot aggregates, (b) 3-D image of a single soot aggregate.
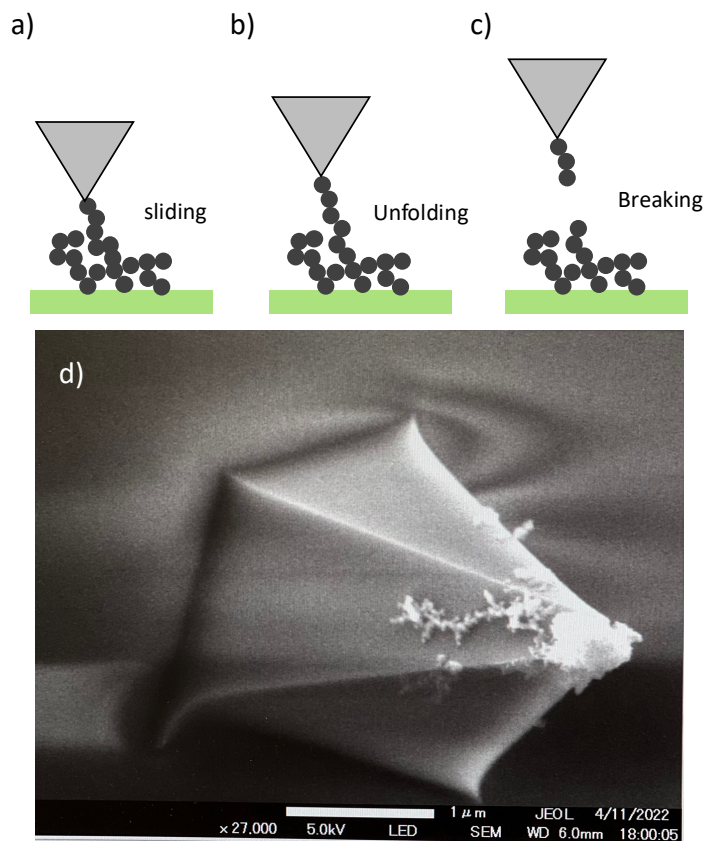
Figure 5.2 Schematics of the AFM experiment. The AFM tip is brought into contact with the aggregate on the surface of the silicon substrate (a). During the approach, aggregate becomes attached to the tip (d), and it is stretched and ruptured during the tip retraction (b) and (c).

5.1 Fractal Soot Aggregates

Figure 5.3a is an example of the force-displacement measurement on bare fractal soot aggregates, showing a typical sawtooth profile observed during retraction of the AFM tip from aggregate. Multiple events forming a sawtooth pattern were always observed during the retraction portion of the measurement. We hypothesize that the sawtooth profile corresponds to the stretch and sequential sliding, unfolding, and eventual breaking of a single aggregate pulled by the tip. The distribution of these peaks, the differences between each maximum and the following minimum in the force-displacement curve of measurements for 100 different aggregates, is plotted as a histogram (Figure 5.3b). For

bare soot, the peaks in the distribution of forces are at 0.18, 0.41, and 0.84 nN, corresponding to sliding, unfolding, and breaking in a single aggregate (Rong et al., 2004).
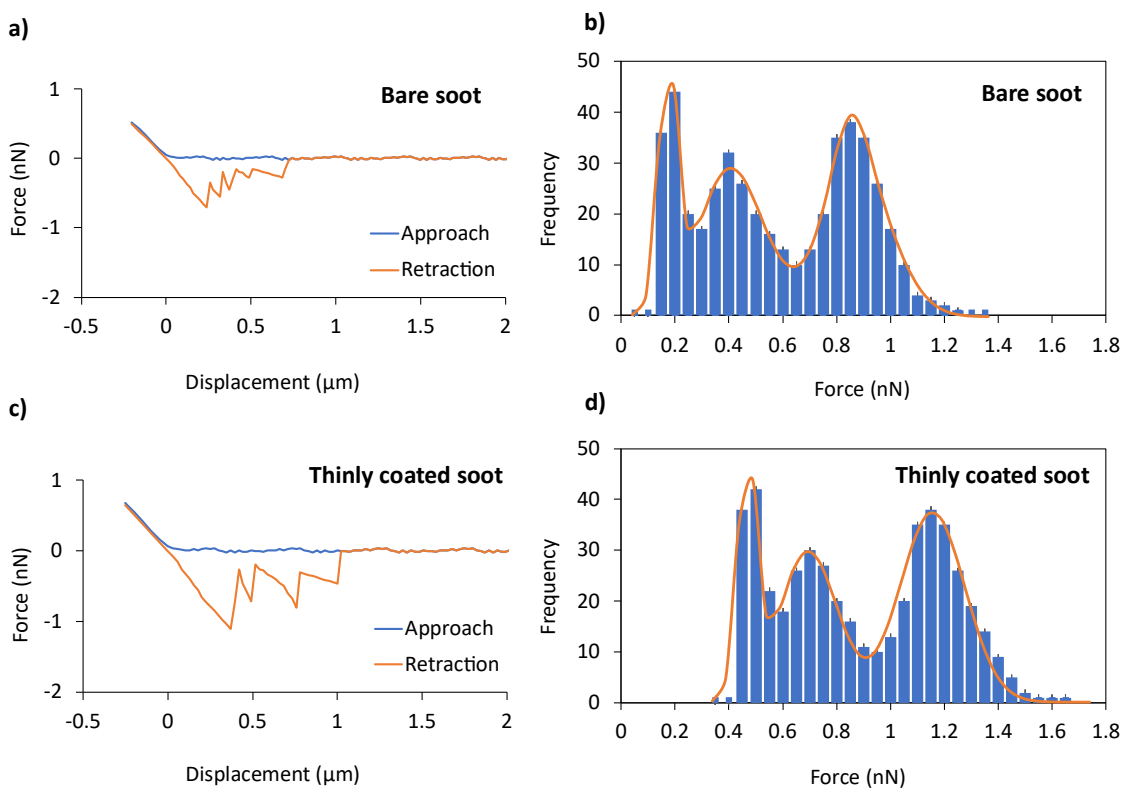
Figure 5.3 Typical force vs displacement curve recorded as the AFM tip approaches and retracts from bare and thinly coated soot aggregate. Multiple rupture events forming a sawtooth pattern were always observed during the retraction portion of the measurement. (a) A typical force curve on bare soot aggregate. (b) A histogram of the forces observed in force curves measured on bare soot aggregates in 100 experiments. The peaks in the distribution of forces are at 0.18, 0.41, and 0.84 nN. (c) Typical force curve on the thinly coated soot aggregate (Gfm = 1.09). (d) A histogram of the forces observed in force curves measured on the on the thinly coated soot aggregates in 100 experiments. Three populations of forces are seen here at 0.48, 0.71, and 1.17 nN.

Figure 5.3c is an example of the force-displacement measurement on soot aggregates thinly coated with dioctyl sebacate (DOS) (Gfm = 1.09 with the coating thickness of 0.7 nm), showing a typical sawtooth profile observed during retraction of the

AFM tip from aggregate. Like for bare aggregate, multiple events forming a sawtooth pattern were always observed during the retraction portion of the measurement. The distribution of these peaks is plotted as a histogram (Figure 5.3d). Three populations of forces are seen here at 0.48, 0.71, and 1.17 nN, corresponding to sliding, unfolding, and breaking in a single aggregate. In addition to forces, the distributions of displacements from the same experiments are also plotted as a histogram for bare and thinly coated aggregates (Figure 5.5). Observed peaks in the histogram of the displacements for bare soot aggregates are at 0.04, 0.09, and 0.19 μm. The peaks in the distribution of displacements for thinly coated soot aggregates are at 0.16, 0.29, and 0.40 μm. These peaks can be attributed to sliding, unfolding, and breaking in a single aggregate (Rong et al., 2004). We compared the observed peaks in histogram of the displacements and histogram of the forces in the bare and thinly coated soot aggregates (Figure 5.6). A similar increase of the displacements and forces in bare vs thinly coated aggregate (water on TiO_2) has been reported by other groups (Laube et al., 2017; Salameh et al., 2012). In detail, a meniscus is formed between two particles based on the physisorbed coating. As we separate the monomers, solid-solid connections are replaced by solid-liquid-solid connections, and a liquid bridge remains between the monomers that produces resistance force to separating the spheres. Indeed, a new peak at 0.39 μm appears in displacements distribution for thinly coated soot aggregates that was not present in bare soot (Figure 5.5b), probably due the presence of a liquid bridge between monomers that results in increasing the displacements during stretching a single aggregate. So, liquid bridge between monomers not only increases displacements, but also shift forces for sliding, unfolding, and breaking between monomers to the larger values (Figure 5.4).
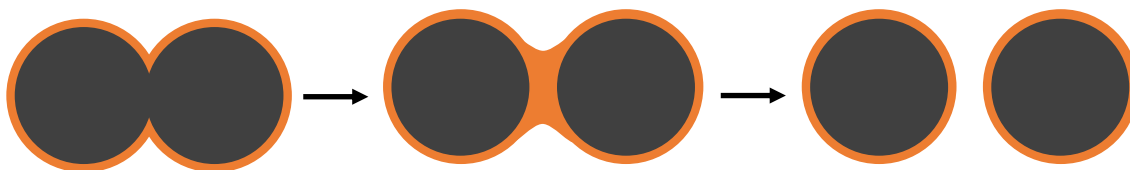
Figure 5.4 Solid-solid connections between the monomers in soot aggregate are replaced by solid-liquid-solid connections. Solid connections may be broken by stretching the aggregate, but liquid (capillary bridge) exists between the monomers, shifts the displacements and forces to larger values.
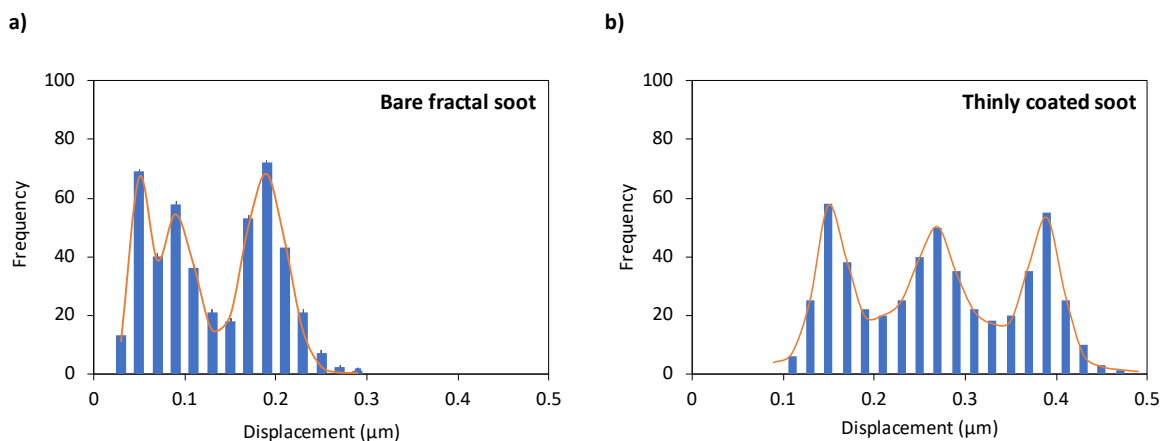
Figure 5.5 Histogram of the displacements observed in force-displacement curves measured on (a) bare soot aggregates in 100 experiments and (b) thinly coated soot aggregates in 100 experiments The peaks in the distribution of displacements for bare soot aggregates are at 0.04, 0.09, and 0.19 μm. The peaks in the distribution of displacements for thinly coated soot aggregates are at 0.16, 0.29, and 0.39 μm.
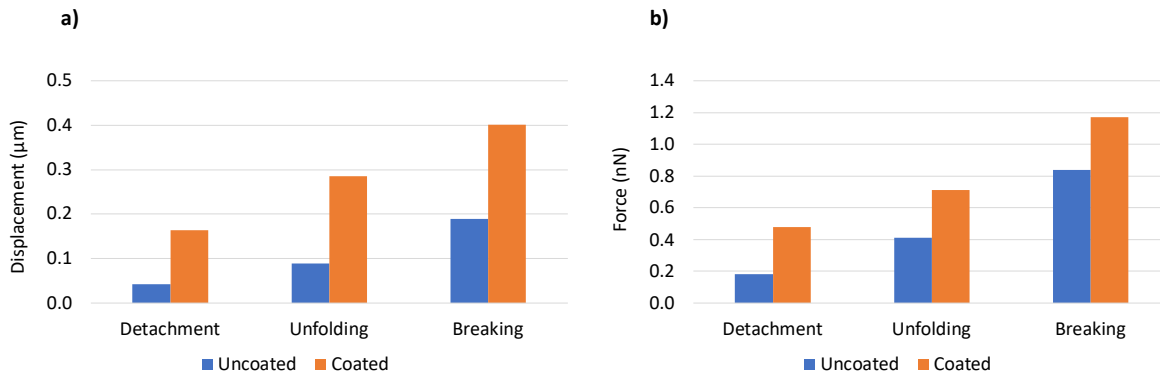
Figure 5.6 Comparison of the observed peaks in (a) histogram of the displacements and (b) histogram of the forces that may correspond to several processes during the stretching/breaking, such as detachments between aggregates, unfolding and breaking the aggregates.

5.2 Bare Compact Soot Aggregates

In this study we also performed force-displacement measurement on bare compact soot aggregates and flat surface of a silicon chip and a graphite plate. Bare compact soot was prepared by encapsulating fresh soot in DOS and removing the coating in thermal denuder, as described in Chapter 4. Next, bare compact soot was collected on flat surface to perform force-displacement measurement (Figure 5.7e). Only single event was observed and it was reproducible in over 100 measurements for different particles. On average we measured a rupture force of 39.9 nN, comparable to the forces observed for the graphitic and silicon surface measurements shown in Figure 5.7c and 5.7a, with the peak in the distribution of forces at 30.6 and 40.5 nN, respectively. This event is due to attraction between the cantilever tip and the compact soot aggregate, graphitic surface, or silicon substrate. Similar observation has been reported by other groups (Alazemi et al., 2020; Rong et al., 2004).
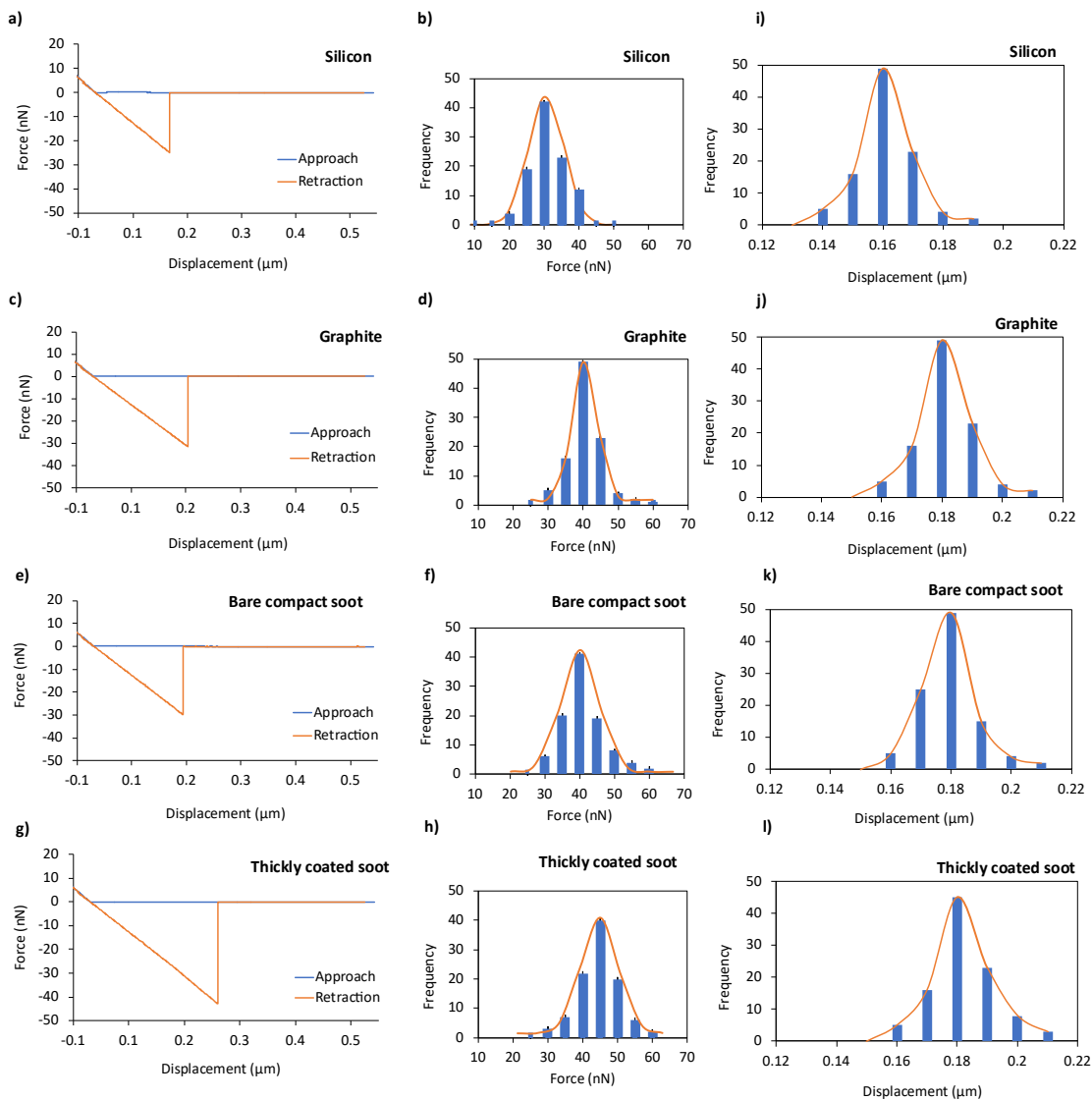
Figure 5.7 Typical force vs displacement curve recorded as the AFM tip approaches and retracts from bare silicon substrate, coated-denuded (compact) soot and thickly coated soot. (a) A typical force curve on bare silicon substrate. (b) Histogram of the forces observed in force curves in 100 measurements on bare silicon substrate. The peak in the distribution of forces is at 30.6 nN. (c) A typical force curve on bare graphite. (d) Histogram of the forces observed in force curves in 100 measurements on bare graphite. The peak in the distribution of forces is at 40.5 nN. (e) A typical force curve on compact soot. (f) Histogram of the forces observed in force curves in 100 measurements on compact soot. The peak in the distribution of forces is at 39.9 nN. (g) Typical force curve on the thickly coated soot aggregate. (h) Histogram of the forces observed in force curves in 100 measurements on thickly coated soot aggregates. The peak in the distribution of forces is at 44.8 nN. Histogram of the displacements in 100 measurements on (i) bare silicon substrate, with the peak in the distribution at 0.16 μm, (j) bare graphite substrate, with the peak in the distribution at 0.18 μm, (k) bare compact soot, with the peak in the distribution at 0.177 μm, and (l) thickly coated soot, with the peak in the distribution at 0.183 μm.

The mechanical properties of material, such as Young's modulus, can be quantified based on the well-established Hertzian model (Ding et al., 2017; Zeng et al., 2018). In this technique, it is assumed that no other interaction than elastic deformation can be observed between tip and sample (Figure 5.8). The calculation is based on the Equation (5.1), assuming F, peak force values from Figure (5.7), and two different tip radii to indent to a displacement of d (Figure 5.7) (Ding et al., 2017). Two different tip radii assumptions are the spherical tip with radius of ~ 100 nm based on Figure (5.2d) and the tip radius specified by the manufacturer ~ 10 nm. With the tip radius of 100 nm, silicon and graphite Young's modulus is 1.1 and 1.3 GPa, respectively. Bare compact and thickly coated soot have Young's modulus of 1.3 and 1.4 GPa, respectively. Considering a sharp tip radius of 10 nm, silicon and graphite Young's modulus increase to 3.6 and 4.0 GPa, respectively. In the literature, Young's modulus of the silicon can be found within the range of 62 to 180 GPa (Hopcroft et al., 2010). Silicon is an anisotropic crystalline material whose material properties depend on orientation relative to the crystal lattice. This fact means that the correct value of Young's modulus for analyzing two different designs in silicon may differ by up to 45%.

Also, considering a sharp tip radius of 10 nm, bare compact and thickly coated soot Young's modulus increases to 4.0 and 4.3 GPa, respectively, which are comparable to the bulk value for graphite (2.1 to 18.6 GPa) (Lynch, 1989). Like silicon, material properties of graphite depend on orientation relative to the crystal lattice, leading to different values of Young's modulus. Also, tip radius was found to have a major impact on the accuracy of measured modulus. The blunt tip with 100 nm radius measured modulus with deviation

from the sharp tip with 10 nm radius up to 300% in different materials as previously reported in another study (Zeng et al., 2018).
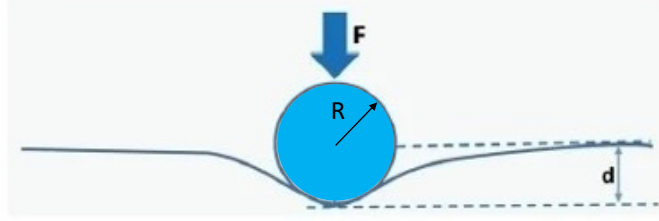
Figure 5.8 Illustration of spherical tip and sample interaction showing the displacement created in the sample surface as force is applied.

$$E = \frac{3}{4} F * \frac{1}{\sqrt{Rd^3}}$$
(5.1)

5.3 Thickly Coated Soot Aggregates

Figure (5.7g) is an example of the force-displacement measurement on thickly coated soot aggregates DOS (Gfm = 3.38 with the coating thickness of 10.9 nm). Like for silicon substrate, graphitic surface, and compact soot only single rupture event was observed and was reproducible in over 100 measurements. On average we measured a rupture force of 44.8 nN. Compared to compact soot, contact forces between cantilever tip and the thickly coated soot increased because of the coating on the aggregate, which can be described by capillary forces (Salameh et al., 2017). Recently, molecular dynamics simulation has been used to study the pull-off force in the nanocontact of two substrates with a small amount of water adsorbed between them (Valenzuela, 2020). It was demonstrated that the pull-off force between two hydrophilic surfaces is entirely dominated by water adsorbed on one of the surfaces. Indeed, water molecules wet the border, with a strong effect on the pull-off force due to the creation of monolayers during the pull-off. These results improve the

interpretation of experimental results of pull-off at low relative humidity for hydrophilic surfaces (Valenzuela, 2020).

Estimation of Young's Modulus for fractal aggregates

In this study we also estimated the Young's modulus of the aggregates based on a method used by Rong et al. (2004). With the difference that they did measurements on a film of chain aggregates, while our case is single aggregate, and all forces correspond to internal motions in a single aggregate. As shown in Figure (5.9), the slope of the curve during stretching, which may be related to the overall elastic constant of the aggregates under tension, decreases gradually from region A to D. The last slope, slope D, in the sawtooth region may show breaking of the connection between monomers and make it possible to estimate the Young's modulus of a single aggregate (Figure 5.9). The distance between the starting point of slope D and the surface of the substrate can be viewed as the original length (L_0) of the aggregate. The length change (δ) can be estimated from the displacement of the AFM tip during the aggregate stretch. The Young's modulus, E, of aggregates can be estimated by dividing the stress, σ, by the strain, ε. Stress is defined by dividing the applied load, F, to the monomers cross-sectional area, A, and d is the half diameter of the graphitic monomers in the soot aggregates (Rong et al., 2004). Figure (5.10a) shows the distribution of Young's modulus in this study for 100 different aggregates. The peak of this distribution increases from 21.7 to 26.3 MPa for bare fractal to thinly coated soot, assuming half diameter in contact area between monomers ($d = 14$ nm). This method has been used previously in another study to calculate the Young's modulus of single-fixed and double-fixed double-stranded deoxyribonucleic acid (dsDNA) (Nguyen et al., 2010). The corresponding Young's modulus of the DNA molecules calculated from the pull-off

lengths, stretch lengths and stretch forces. As a result, the Young's modulus of the double-fixed dsDNA (60 MPa) was greater than that of the single-fixed (45 MPa) (Nguyen et al., 2010).

$$E = \frac{\sigma}{\epsilon} = \frac{\dfrac{F}{A}}{\dfrac{\delta}{L_0}} = \frac{\dfrac{F}{\dfrac{\pi d^2}{4}}}{\dfrac{\delta}{L_0}} = \frac{4FL_0}{\pi \delta d^2}$$
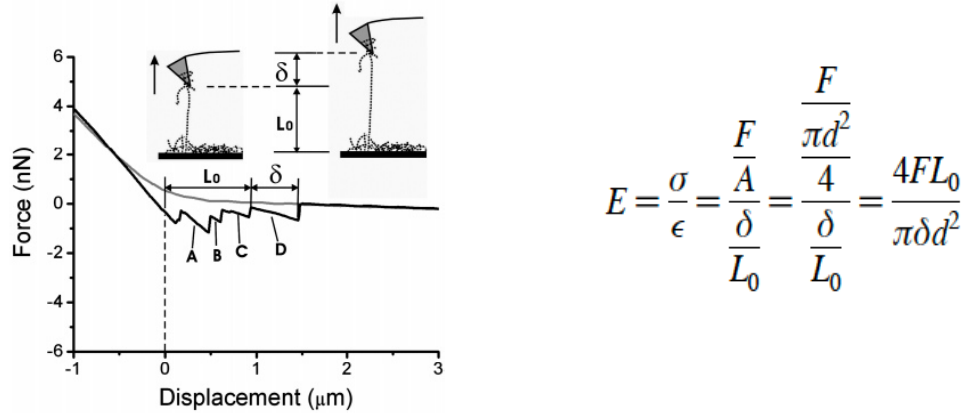
Figure 5.9 Estimation of the Young's modulus of aggregates using the force vs displacement curve. A, B, C, and D indicate the slopes in the curve. The original length (L_0) and length change (δ) of the chain are labeled on curves and schematics.

Using the same approach described by Rong et al. (2004), but in opposite way, we calculated the diameter in contact area between the monomers by assuming solid graphite Young's modulus 4 GPa, within the range of the reported values for graphite (Lynch, 1989). Figure (5.10b) shows the distributions of 100 measurements of the diameter in contact area between monomers in bare fractal and thinly coated soot, with maxima at 1.03 to 1.19 nm. We used solid graphitic modulus to get the diameter in contact, so it is not surprising that d increased a little bit. With the thinly coated soot, solid-solid connections are replaced by solid-liquid-solid connections. As we separate the monomers a liquid bridge remains between the monomers that produces resistance force to separating the spheres (Figure 5.4).

a)

b)
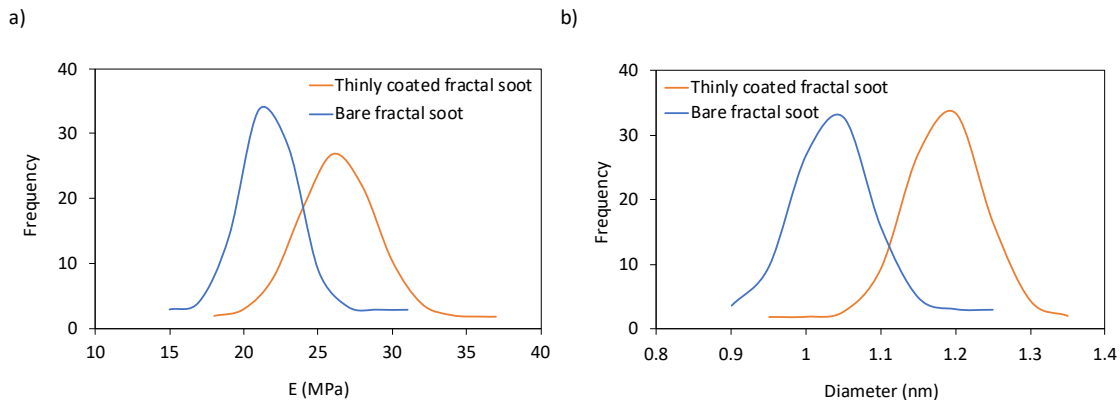
Figure 5.10 a) Young's modulus of bare fractal and thinly coated soot, increases from 21.7 to 26.3 MPa, assuming half diameter in contact area between monomers. b) diameter of the contact area between monomers in bare fractal and thinly coated soot, increases from 1.03 to 1.19 nm, assuming graphite Young's modulus 4 Gpa.

To conclude this chapter, observed peaks in the distributions of forces for bare soot may be related to the processes that occur during aggregate stretching, such as detachments between the monomers, unfolding, and breaking of the connections between monomers. These forces were significantly affected in the presence of a condensate. In thickly coated and bare compact soot, retraction forces resemble separation of the AFM tip from a solid surface, because when the connections between monomers are broken and soot becomes compact, it behaves as a solid surface.

CONCLUSIONS

In this dissertation, we elucidated and quantified the factors that control restructuring of combustion soot nanoparticles. Relative roles of vapor condensation and coating evaporation on soot restructuring have been investigated. We showed that wetting and non-wetting liquids act differently in soot restructuring. For the liquids capable of wetting the surface of soot aggregates, minor restructuring begins already during capillary condensation and significant restructuring occurs as the coating volume increases. With non-wetting liquids, such as water, it is the evaporation that drives most of restructuring and there is almost no restructuring during condensation.

We investigated interaction of thinly coated soot particles with water vapor and determined the role of the subsaturated and supersaturated water vapor on restructuring of coated soot aggregates. Soot can get fully encapsulated and restructured upon exposure to supersaturated water vapor, if the particles are primed with a monolayer of a hydrophilic chemical. However, those primed soot particles restructured significantly even in exposure to subsaturated water vapor. Under subsaturated conditions capillary condensation of hygroscopic chemicals can occur into the junctions between carbon spherules, driven by the saturation pressure depression caused by the concave meniscus. Furthermore, the concave meniscus promotes absorption of a significant amount of water vapor by the condensate at moderate relative humidities, exceeding the amounts achievable for flat and convex surfaces. Exposure of fractal soot particles to subsaturated vapors of hygroscopic chemicals in the atmosphere may be an important route towards soot compaction even at moderate relative humidities.

We used AFM to study the mechanical properties of soot aggregates by measuring force-displacement curves of soot aggregates subjected to different processing: bare fractal, thinly coated fractal, thickly coated, and bare compact. We investigated the interaction forces between the monomers in the soot aggregates. Observed peaks in the distributions of forces for bare soot, may be related to the processes that occur during aggregate stretching, such as detachments between the monomers, unfolding, and breaking of the connections between monomers. These forces were significantly affected in the presence of a condensate. In thickly coated and bare compact soot, retraction forces resemble separation of the AFM tip from a solid surface, because when the connections between monomers are broken and soot becomes compact, it behaves as a solid surface. These results are expected to contribute to the development of mathematical models for soot restructuring.

REFERENCES

Alazemi, A. A., Dysart, A. D., & Pol, V. G. (2020). Experimental investigation of the mechanical and surface properties of sub-micron carbon spheres. *Lubricants*, *8*(7), 77.

Barone, A. C., D'Alessio, A., & D'Anna, A. (2003). Morphological characterization of the early process of soot formation by atomic force microscopy. *Combustion and Flame 132*(1–2), 181-187. https://doi.org/http://dx.doi.org/10.1016/S0010-2180(02)00434-0

Bento, D. S., Thomson, K. A., & Gulder, O. L. (2006). Soot formation and temperature field structure in laminar propane-air diffusion flames at elevated pressures. *Combustion and Flame 145*(4), 765-778. https://doi.org/10.1016/j.combustflame.2006.01.010

Bhandari, J., China, S., Chandrakar, K. K., Kinney, G., Cantrell, W., Shaw, R. A., Mazzoleni, L. R., Girotto, G., Sharma, N., Gorkowski, K., Gilardoni, S., Decesari, S., Facchini, M. C., Zanca, N., Pavese, G., Esposito, F., Dubey, M. K., Aiken, A. C., Chakrabarty, R. K., Moosmüller, H., Onasch, T. B., Zaveri, R. A., Scarnato, B. V., Fialho, P., & Mazzoleni, C. (2019). Extensive Soot Compaction by Cloud Processing from Laboratory and Field Observations. *Scientific Reports*, *9*(1), 11824. https://doi.org/10.1038/s41598-019-48143-y

Bilde, M., Svenningsson, B., Monster, J., & Rosenorn, T. (2003). Even-odd alternation of evaporation rates and vapor pressures of C3-C9 dicarboxylic acid aerosols. *Environmental Science and Technology*, *37*(7), 1371-1378. https://doi.org/10.1021/es0201810

Boatman, R. J., & Knaak, J. B. (2001). Ethers of ethylene glycol and derivatives. *Patty's toxicology*.

Burnett, R. T., Pope III, C. A., Ezzati, M., Olives, C., Lim, S. S., Mehta, S., Shin, H. H., Singh, G., Hubbell, B., & Brauer, M. (2014). An integrated risk function for estimating the global burden of disease attributable to ambient fine particulate matter exposure. *Environmental health perspectives*, *122*(4), 397-403.

Bzdek, B. R., & Johnston, M. V. (2010). New Particle Formation and Growth in the Troposphere [doi: 10.1021/ac100856j]. *Analytical Chemistry 82*(19), 7871-7878. https://doi.org/10.1021/ac100856j

Chakrabarty, R. K., Garro, M. A., Garro, B. A., Chancellor, S., Moosmüller, H., & Herald, C. M. (2011). Simulation of Aggregates with Point-Contacting Monomers in the Cluster–Dilute Regime. Part 1: Determining the Most Reliable Technique for Obtaining Three-Dimensional Fractal Dimension from Two-Dimensional

Images. *Aerosol Science and Technology 45*(1), 75-80.
http://www.informaworld.com/10.1080/02786826.2010.520363

Chen, C., Enekwizu, O., Ma, Y., Zakharov, D., & Khalizov, A. (2017). The Impact of
Sampling Medium and Environment on Particle Morphology. *Atmosphere*, *8*(9),
162. http://www.mdpi.com/2073-4433/8/9/162

Chen, C., Enekwizu, O. Y., Fan, X., Dobrzanski, C. D., Ivanova, E. V., Ma, Y., Gor, G.
Y., & Khalizov, A. F. (2018). Single Parameter for Predicting the Morphology of
Atmospheric Black Carbon. *Environmental Science & Technology*, *52*(24),
14169-14179. https://doi.org/10.1021/acs.est.8b04201

Chen, C., Fan, X., Shaltout, T., Qiu, C., Ma, Y., Goldman, A., & Khalizov, A. F. (2016).
An unexpected restructuring of combustion soot aggregates by subnanometer
coatings of polycyclic aromatic hydrocarbons. *Geophysical Research Letters*,
43(20), 11,080-011,088. https://doi.org/10.1002/2016GL070877

Cheng, T., Wu, Y., & Chen, H. (2014). Effects of morphology on the radiative properties
of internally mixed light absorbing carbon aerosols with different aging status.
Optics Express, *22*(13), 15904-15917.
http://www.scopus.com/inward/record.url?eid=2-s2.0-
84903743585&partnerID=40&md5=0b0e5dde28586f4d8d4bb297abc5e3d2

China, S., Mazzoleni, C., Gorkowski, K., Aiken, A. C., & Dubey, M. K. (2013).
Morphology and mixing state of individual freshly emitted wildfire carbonaceous
particles. *Nature Communications*, *4*, 2122.
http://www.scopus.com/inward/record.url?eid=2-s2.0-
84881351484&partnerID=40&md5=1c8cf3ae2bbdb5ab04f41bbed5bcdaed

China, S., Scarnato, B., Owen, R. C., Zhang, B., Ampadu, M. T., Kumar, S., Dzepina, K.,
Dziobak, M. P., Fialho, P., Perlinger, J. A., Hueber, J., Helmig, D., Mazzoleni, L.
R., & Mazzoleni, C. (2015). Morphology and mixing state of aged soot particles
at a remote marine free troposphere site: Implications for optical properties.
Geophysical Research Letters, *42*(4), 1243-1250.
https://doi.org/10.1002/2014GL062404

Daubert, T. E. (1989). Physical and thermodynamic properties of pure chemicals: data
compilation. *Design Institute for Physacal Property Data (DIPPR)*.

DeCarlo, P. F., Slowik, J. G., Worsnop, D. R., Davidovits, P., & Jimenez, J. L. (2004).
Particle morphology and density characterization by combined mobility and
aerodynamic diameter measurements. Part 1: Theory. *Aerosol Science and
Technology 38*(12), 1185-1205. https://doi.org/10.1080/027868290903907

Ding, Y., Xu, G.-K., & Wang, G.-F. (2017). On the determination of elastic moduli of
cells by AFM based indentation. *Scientific reports*, *7*(1), 1-8.

Dionne, B., Rounbehler, D., Achter, E., Hobbs, J., & Fine, D. (1986). Vapor pressure of explosives. *Journal of Energetic Materials*, *4*(1-4), 447-472.

Dixkens, J., & Fissan, H. (1999). Development of an Electrostatic Precipitator for Off-Line Particle Analysis. *Aerosol Science and Technology*, *30*(5), 438-453. https://doi.org/10.1080/027868299304480

Doner, N., Liu, F., & Yon, J. (2017). Impact of necking and overlapping on radiative properties of coated soot aggregates. *Aerosol Science and Technology*, *51*(4), 532-542. https://doi.org/10.1080/02786826.2016.1275513

Ebert, M., Inerle-Hof, M., & Weinbruch, S. (2002). Environmental scanning electron microscopy as a new technique to determine the hygroscopic behaviour of individual aerosol particles. *Atmospheric Environment*, *36*(39–40), 5909-5916. https://doi.org/http://dx.doi.org/10.1016/S1352-2310(02)00774-4

Ehara, K., Hagwood, C., & Coakley, K. J. (1996). Novel method to classify aerosol particles according to their mass-to-charge ratio - Aerosol particle mass analyser. *Journal of Aerosol Science*, *27*(2), 217-234. <Go to ISI>://A1996UF69200003

Enekwizu, O. Y., Hasani, A., & Khalizov, A. F. (2021). Vapor Condensation and Coating Evaporation Are Both Responsible for Soot Aggregate Restructuring. *Environmental Science & Technology*.

Green, D. W., & Perry, R. H. (2008). *Perry's chemical engineers' handbook*. McGraw-Hill Education.

Guide, D. G. P. The MEGlobal Group of Companies: 2005. *Google Scholar There is no corresponding record for this reference*.

He, C. (2019). Radiative properties of atmospheric black carbon (soot) particles with complex structures. In *Springer Series in Light Scattering* (pp. 219-254). Springer.

Hopcroft, M. A., Nix, W. D., & Kenny, T. W. (2010). What is the Young's Modulus of Silicon? *Journal of microelectromechanical systems*, *19*(2), 229-238.

Ivanova, E. V., Khalizov, A. F., & Gor, G. Y. (2020). Kinetic model for competitive condensation of vapor between concave and convex surfaces in a soot aggregate. *Aerosol Science and Technology*, *55*(3), 1-19. https://doi.org/10.1080/02786826.2020.1846677

Johansson, K. O., Head-Gordon, M. P., Schrader, P. E., Wilson, K. R., & Michelsen, H. A. (2018). Resonance-stabilized hydrocarbon-radical chain reactions may explain soot inception and growth. *Science*, *361*(6406), 997-1000. https://doi.org/10.1126/science.aat3417

Johansson, K. O., Lai, J. Y. W., Skeen, S. A., Popolan-Vaida, D. M., Wilson, K. R., Hansen, N., Violi, A., & Michelsen, H. A. (2015). Soot precursor formation and limitations of the stabilomer grid. *Proceedings of the Combustion Institute*, *35*(2), 1819-1826. https://doi.org/http://dx.doi.org/10.1016/j.proci.2014.05.033

Kahnert, M., Nousiainen, T., & Lindqvist, H. (2014). Review: Model particles in atmospheric optics. *Journal of Quantitative Spectroscopy and Radiative Transfer*, *146*(0), 41-58. https://doi.org/http://dx.doi.org/10.1016/j.jqsrt.2014.02.014

Khalizov, A. F., Zhang, R., Zhang, D., Xue, H., Pagels, J., & McMurry, P. H. (2009). Formation of highly hygroscopic soot aerosols upon internal mixing with sulfuric acid vapor. *Journal of Geophysical Research*, *114*, D05208. https://doi.org/10.1029/2008JD010595

Koehler, K. A., DeMott, P. J., Kreidenweis, S. M., Popovicheva, O. B., Petters, M. D., Carrico, C. M., Kireeva, E. D., Khokhlova, T. D., & Shonija, N. K. (2009). Cloud condensation nuclei and ice nucleation activity of hydrophobic and hydrophilic soot particles. *Physical Chemistry Chemical Physics 11*(36), 7906-7920. http://dx.doi.org/10.1039/b905334b

Kolb, C. E., & Worsnop, D. R. (2012). Chemistry and composition of atmospheric aerosol particles. *Annual review of physical chemistry*, *63*, 471-491.

Köllensperger, G., Friedbacher, G., Kotzick, R., Niessner, R., & Grasserbauer, M. (1999). In-situ atomic force microscopy investigation of aerosols exposed to different humidities. *Fresenius' Journal of Analytical Chemistry*, *364*(4), 296-304. http://www.scopus.com/inward/record.url?eid=2-s2.0-0000402969&partnerID=40&md5=d4c05e8f849c2cf92d021c43f51e8531

Kütz, S., & Schmidt-Ott, A. (1992). Characterization of agglomerates by condensation-induced restructuring. *Journal of Aerosol Science 23*(Supplement 1), 357-360. http://www.sciencedirect.com/science/article/B6V6B-487FB41-3X/2/9175a0183833f9c50dfa3601d2a5ce78

Laube, J., Dörmann, M., Schmid, H.-J., Mädler, L., & Colombi Ciacchi, L. (2017). Dependencies of the Adhesion Forces between TiO2 Nanoparticles on Size and Ambient Humidity. *The Journal of Physical Chemistry C*, *121*(28), 15294-15303. https://doi.org/10.1021/acs.jpcc.7b05655

Liati, A., Brem, B. T., Durdina, L., Vögtli, M., Arroyo Rojas Dasilva, Y., Dimopoulos Eggenschwiler, P., & Wang, J. (2014). Electron microscopic study of soot particulate matter emissions from aircraft turbine engines. *Environmental science & technology*, *48*(18), 10975-10983.

Liu, D., Whitehead, J., Alfarra, M. R., Reyes-Villegas, E., Spracklen, D. V., Reddington, C. L., Kong, S., Williams, P. I., Ting, Y.-C., Haslett, S., Taylor, J. W., Flynn, M. J., Morgan, W. T., McFiggans, G., Coe, H., & Allan, J. D. (2017). Black-carbon

absorption enhancement in the atmosphere determined by particle mixing state [Article]. *Nature Geosci*, *10*(3), 184-188. https://doi.org/10.1038/ngeo2901

Lopez-Hilfiker, F., Mohr, C., Ehn, M., Rubach, F., Kleist, E., Wildt, J., Mentel, T. F., Lutz, A., Hallquist, M., & Worsnop, D. (2014). A novel method for online analysis of gas and particle composition: description and evaluation of a Filter Inlet for Gases and AEROsols (FIGAERO). *Atmospheric Measurement Techniques*, *7*(4), 983-1001.

Lynch, C. T. (1989). *Practical handbook of materials science*. CRC press, Inc., 2000 Corporate Blvd., N.W., Boca Raton, Florida, 33431.

Ma, X., Zangmeister, C. D., Gigault, J., Mulholland, G. W., & Zachariah, M. R. (2013). Soot aggregate restructuring during water processing. *Journal of Aerosol Science*, *66*(0), 209-219. https://doi.org/http://dx.doi.org/10.1016/j.jaerosci.2013.08.001

Ma, Y., Li, S., Zheng, J., Khalizov, A., Wang, X., Wang, Z., & Zhou, Y. (2017). Size-resolved measurements of mixing state and cloud-nucleating ability of aerosols in Nanjing, China. *Journal of Geophysical Research: Atmospheres*, *122*(17), 9430-9450. https://doi.org/doi:10.1002/2017JD026583

McMurry, P. H., Wang, X., Park, K., & Ehara, K. (2002). The relationship between mass and mobility for atmospheric particles: A new technique for measuring particle density. *Aerosol Science and Technology 36*(2), 227-238. <Go to ISI>://000173865200012

Mikhailov, E. F., Vlasenko, S. S., Kramer, L., & Niessner, R. (2001). Interaction of soot aerosol particles with water droplets: influence of surface hydrophilicity. *Journal of Aerosol Science*, *32*(6), 697-711. <Go to ISI>://000168589500001

Miyahara, K., Nagashima, N., Ohmura, T., & Matsuoka, S. (1999). Evaluation of mechanical properties in nanometer scale using AFM-based nanoindentation tester. *Nanostructured Materials*, *12*(5–8), 1049-1052. https://doi.org/http://dx.doi.org/10.1016/S0965-9773(99)00297-4

Moore, S., Keyser, L., Leu, M., Turco, R., & Smith, R. (1990). Heterogeneous reactions on nitric acid trihydrate. *Nature*, *345*(6273), 333-335.

Nguyen, T.-H., Lee, S.-M., Na, K., Yang, S., Kim, J., & Yoon, E.-S. (2010). An improved measurement of dsDNA elasticity using AFM. *Nanotechnology*, *21*(7), 075101.

Onda, T., Shibuichi, S., Satoh, N., & Tsujii, K. (1996). Super-water-repellent fractal surfaces. *Langmuir*, *12*(9), 2125-2127.

Pagels, J., Khalizov, A. F., McMurry, P. H., & Zhang, R. Y. (2009). Processing of Soot by Controlled Sulphuric Acid and Water Condensation-Mass and Mobility

Relationship. *Aerosol Science and Technology 43*(7), 629 - 640. http://www.informaworld.com/10.1080/02786820902810685

Park, K., Cao, F., Kittelson, D. B., & McMurry, P. H. (2003). Relationship between particle mass and mobility for diesel exhaust particles. *Environmental Science and Technology*, *37*(3), 577-583. <Go to ISI>://000180791100035

Pršlja, P., Lomba, E., Gómez-Álvarez, P., Urbič, T., & Noya, E. G. (2019). Adsorption of water, methanol, and their mixtures in slit graphite pores. *The Journal of Chemical Physics*, *150*(2), 024705.

Radney, J. G., You, R., Ma, X., Conny, J. M., Zachariah, M. R., Hodges, J. T., & Zangmeister, C. D. (2014). Dependence of Soot Optical Properties on Particle Morphology: Measurements and Model Comparisons. *Environmental Science & Technology*, *48*(6), 3169-3176. https://doi.org/10.1021/es4041804

Ramirez-Aguilar, K. A., Lehmpuhl, D. W., Michel, A. E., Birks, J. W., & Rowlen, K. L. (1999). Atomic force microscopy for the analysis of environmental particles. *Ultramicroscopy*, *77*(3-4), 187-194. https://doi.org/10.1016/s0304-3991(99)00048-0

Rong, W., Pelling, A. E., Ryan, A., Gimzewski, J. K., & Friedlander, S. K. (2004). Complementary TEM and AFM Force Spectroscopy to Characterize the Nanomechanical Properties of Nanoparticle Chain Aggregates. *Nano Letters*, *4*(11), 2287-2292. https://doi.org/10.1021/nl0487368

Salameh, S., Schneider, J., Laube, J., Alessandrini, A., Facci, P., Seo, J. W., Ciacchi, L. C., & Mädler, L. (2012). Adhesion Mechanisms of the Contact Interface of TiO2 Nanoparticles in Films and Aggregates. *Langmuir*, *28*(31), 11457-11464. https://doi.org/10.1021/la302242s

Salameh, S., Van Der Veen, M. A., Kappl, M., & Van Ommen, J. R. (2017). Contact forces between single metal oxide nanoparticles in gas-phase applications and processes. *Langmuir*, *33*(10), 2477-2484.

Scarnato, B. V., Vahidinia, S., Richard, D. T., & Kirchstetter, T. W. (2013). Effects of internal mixing and aggregate morphology on optical properties of black carbon using a discrete dipole approximation model. *Atmospheric Chemistry and Physics 13*(10), 5089-5101. https://doi.org/10.5194/acp-13-5089-2013

Schnitzler, E. G., Dutt, A., Charbonneau, A. M., Olfert, J. S., & Jäger, W. (2014). Soot Aggregate Restructuring Due to Coatings of Secondary Organic Aerosol Derived from Aromatic Precursors. *Environmental Science & Technology*, *48*(24), 14309-14316. https://doi.org/10.1021/es503699b

Schnitzler, E. G., Gac, J. M., & Jäger, W. (2017). Coating surface tension dependence of soot aggregate restructuring. *Journal of Aerosol Science*, *106*, 43-55. https://doi.org/http://dx.doi.org/10.1016/j.jaerosci.2017.01.005

Seinfeld, J. H., & Pandis, S. N. (1998). *Atmospheric chemistry and physics: from air pollution to climate change*. John Wiley.

Slowik, J. G., Cross, E. S., Han, J. H., Kolucki, J., Davidovits, P., Williams, L. R., Onasch, T. B., Jayne, J. T., Kolb, C. E., & Worsnop, D. R. (2007). Measurements of morphology changes of fractal soot particles using coating and denuding experiments: Implications for optical absorption and atmospheric lifetime. *Aerosol Science and Technology*, *41*(8), 734-750. <Go to ISI>://000248575900002

Sorensen, C. M. (2001). Light Scattering by Fractal Aggregates: A Review. *Aerosol Science and Technology 35*(2), 648 - 687. http://www.informaworld.com/10.1080/02786820117868

Sorensen, C. M. (2011). The Mobility of Fractal Aggregates: A Review. *Aerosol Science and Technology 45*(7), 765-779. https://doi.org/10.1080/02786826.2011.560909

Sorensen, C. M., Yon, J., Liu, F., Maughan, J., Heinson, W. R., & Berg, M. J. (2018). Light scattering and absorption by fractal aggregates including soot. *Journal of Quantitative Spectroscopy and Radiative Transfer*, *217*, 459-473.

Swarup, C., Gourihar, K., Barbara, V. S., Noopur, S., Mikhail, P., John, E. S., Jacqueline, W., Alla, Z., Duli, C., Shang, L., Allison, C. A., Manvendra, D., Alexander, L., Rahul, A. Z., & Claudio, M. (2015). Morphology of diesel soot residuals from supercooled water droplets and ice crystals: implications for optical properties. *Environmental Research Letters*, *10*(11), 114010. http://stacks.iop.org/1748-9326/10/i=11/a=114010

Taleb, D.-E., Ponche, J.-L., & Mirabel, P. (1996). Vapor pressures in the ternary system water-nitric acid-sulfuric acid at low temperature: A reexamination [https://doi.org/10.1029/96JD02330]. *Journal of Geophysical Research: Atmospheres*, *101*(D20), 25967-25977. https://doi.org/https://doi.org/10.1029/96JD02330

Tang, I. N. (1996). Chemical and size effects of hygroscopic aerosols on light scattering coefficients. *Journal of Geophysical Research: Atmospheres*, *101*(D14), 19245-19250.

Tritscher, T., Juranyi, Z., Martin, M., Chirico, R., Gysel, M., Heringa, M. F., DeCarlo, P. F., Sierau, B., Prevot, A. S. H., Weingartner, E., & Baltensperger, U. (2011). Changes of hygroscopicity and morphology during ageing of diesel soot. *Environmental Research Letters*, *6*(3), Article 034026. https://doi.org/10.1088/1748-9326/6/3/034026

Twohy, C. H., & Anderson, J. R. (2008). Droplet nuclei in non-precipitating clouds: composition and size matter. *Environmental Research Letters*, *3*(4). https://doi.org/045002, 10.1088/1748-9326/3/4/045002

Valenzuela, G. E. (2020). Roughness Effect on the Pull-Off Force between Two Surfaces with Water Adsorbed between Them. A Molecular Dynamics Simulation Perspective. *The Journal of Physical Chemistry C*, *124*(15), 8210-8217.

Weingartner, E., Baltensperger, U., & Burtscher, H. (1995). Growth and structural-change of combustion aerosols at high relative-humidity. *Environmental Science & Technology*, *29*(12), 2982-2986. https://doi.org/10.1021/es00012a014

Wise, M. E., Surratt, J. D., Curtis, D. B., Shilling, J. E., & Tolbert, M. A. (2003). Hygroscopic growth of ammonium sulfate/dicarboxylic acids. *Journal of Geophysical Research: Atmospheres*, *108*(D20).

Wu, L., Li, X., & Ro, C.-U. (2019). Hygroscopic behavior of ammonium sulfate, ammonium nitrate, and their mixture particles. *Asian Journal of Atmospheric Environment*, *13*(3), 196-211.

Xu, L., Fukushima, S., Sobanska, S., Murata, K., Naganuma, A., Liu, L., Wang, Y., Niu, H., Shi, Z., & Kojima, T. (2020). Tracing the evolution of morphology and mixing state of soot particles along with the movement of an Asian dust storm. *Atmospheric Chemistry and Physics*, *20*(22), 14321-14332.

Xue, H., Khalizov, A. F., Wang, L., Zheng, J., & Zhang, R. (2009). Effects of Coating of Dicarboxylic Acids on the Mass-Mobility Relationship of Soot Particles. *Environmental Science & Technology*, *43*(8), 2787-2792. https://doi.org/doi:10.1021/es803287v

Yaws, C. (1998). *Chemical Properties Handbook: Physical, Thermodynamics, Environmental Transport, Safety & Health Related Properties for Organic & Inorganic Chemicals*.

Yon, J., Ouf, F.-X., Hebert, D., Mitchell, J. B., Teuscher, N., Le Garrec, J.-L., Bescond, A., Baumann, W., Ourdani, D., & Bizien, T. (2018). Investigation of soot oxidation by coupling LII, SAXS and scattering measurements. *Combustion and Flame*, *190*, 441-453.

Young, T., & Grinstead, S. (1949). The surface tensions of aqueous sulfuric acid solutions. *Annals of the New York Academy of Sciences*, *51*(4), 765-780.

Yuan, C., Zheng, J., Ma, Y., Jiang, Y., Li, Y., & Wang, Z. (2020). Significant restructuring and light absorption enhancement of black carbon particles by ammonium nitrate coating. *Environmental Pollution*, *262*, 114172. https://doi.org/https://doi.org/10.1016/j.envpol.2020.114172

Zelenyuk, A., & Imre, D. (2005). Single particle laser ablation time-of-flight mass spectrometer: an introduction to SPLAT. *Aerosol Science and Technology*, *39*(6), 554-568.

Zeng, G., Dirscherl, K., & Garnæs, J. (2018). Toward accurate quantitative elasticity mapping of rigid nanomaterials by atomic force microscopy: effect of acquisition frequency, loading force, and tip geometry. *Nanomaterials*, *8*(8), 616.

Zhang, D., & Zhang, R. (2005). Laboratory Investigation of Heterogeneous Interaction of Sulfuric Acid with Soot. *Environ. Sci. Technol.*, *39*(15), 5722-5728. http://pubs3.acs.org/acs/journals/doilookup?in_doi=10.1021/es050372d

Zhang, R., Khalizov, A. F., Pagels, J., Zhang, D., Xue, H., & McMurry, P. H. (2008). Variability in morphology, hygroscopicity, and optical properties of soot aerosols during atmospheric processing. *Proceedings of the National Academy of Sciences of the United States of America*, *105*(30), 10291-10296. https://doi.org/10.1073/pnas.0804860105

Zhao, Y., & Ma, L. (2009). Assessment of two fractal scattering models for the prediction of the optical characteristics of soot aggregates. *Journal of Quantitative Spectroscopy and Radiative Transfer*, *110*(4–5), 315-322. https://doi.org/http://dx.doi.org/10.1016/j.jqsrt.2008.12.002

Zhou, Q., Cheng, C., Yang, S., Yuan, M., Meng, J., Gong, H., Zhong, Q., Zhang, Y., Xie, Y., & Zhou, Z. (2022). Enhanced mixing state of black carbon with nitrate in single particles during haze periods in Zhengzhou, China. *Journal of Environmental Sciences*, *111*, 185-196.

Zuberi, B., Johnson, K. S., Aleks, G. K., Molina, L. T., & Laskin, A. (2005). Hydrophilic properties of aged soot. *Geophysical Research Letters*, *32*(1), L01807. <Go to ISI>://000226510800003